

Accepted Manuscript

Biocompatible hybrids based on nanographene oxide covalently linked to glycolporphyrins: Synthesis, characterization and biological evaluation

Carla I.M. Santos, Gil Gonçalves, Mónica Cicuéndez, Inês Mariz, Virgília S. Silva, Helena Oliveira, Fábio Campos, Sandra I. Vieira, Paula A.A.P. Marques, Ermelinda M.S. Maçôas, M.Graça P.M.S. Neves, José M.G. Martinho

PII: S0008-6223(18)30399-3

DOI: [10.1016/j.carbon.2018.04.040](https://doi.org/10.1016/j.carbon.2018.04.040)

Reference: CARBON 13077

To appear in: *Carbon*

Received Date: 10 January 2018

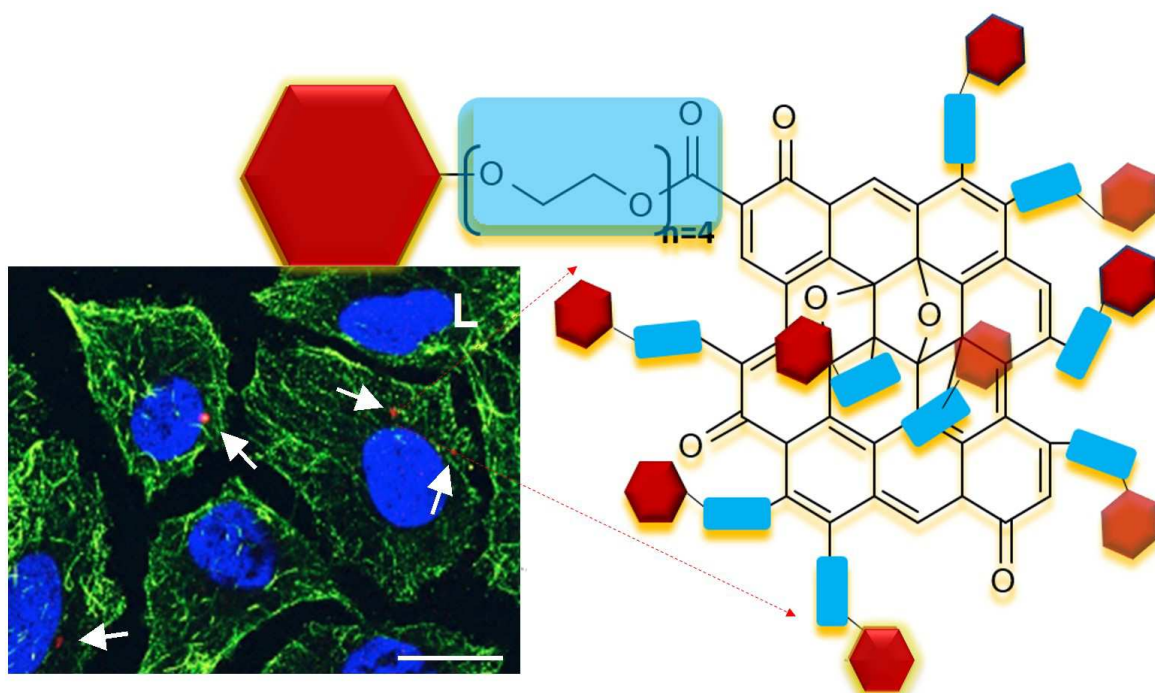
Revised Date: 13 April 2018

Accepted Date: 16 April 2018

Please cite this article as: C.I.M. Santos, G. Gonçalves, M. Cicuéndez, Inês Mariz, Virgília S. Silva, H. Oliveira, Fábio Campos, Sandra I. Vieira, Paula A.A.P. Marques, Ermelinda M.S. Maçôas, M.Graça P.M.S. Neves, José M.G. Martinho, Biocompatible hybrids based on nanographene oxide covalently linked to glycolporphyrins: Synthesis, characterization and biological evaluation, *Carbon* (2018), doi: 10.1016/j.carbon.2018.04.040.

This is a PDF file of an unedited manuscript that has been accepted for publication. As a service to our customers we are providing this early version of the manuscript. The manuscript will undergo copyediting, typesetting, and review of the resulting proof before it is published in its final form. Please note that during the production process errors may be discovered which could affect the content, and all legal disclaimers that apply to the journal pertain.





ACCEPTED MANUSCRIPT

Biocompatible hybrids based on nanographene oxide covalently linked to glycolporphyrins: synthesis, characterization and biological evaluation

*Carla, I. M. Santos,^{a,b*1} Gil Gonçalves^c Mónica Cicuéndez,^{c,d} Inês Mariz,^a Virgília S. Silva,^e Helena Oliveira,^{d,e} Fábio Campos,^e Sandra I. Vieira,^f Paula A. A. P. Marques,^{c*} Ermelinda M. S. Maçôas,^{a*} M. Graça P. M. S. Neves,^b José M. G. Martinho.^a*

^aCQFM, Centro de Química-Física Molecular, IN—Institute of Nanosciences and Nanotechnology, and CQE, Centro de Química Estrutural, Instituto Superior Técnico, Av. Rovisco Pais, 1049-001 Lisboa, Portugal

^bQOPNA, Chemistry Department, University of Aveiro, Campus Universitario de Santiago, 3810-193 Aveiro, Portugal

^cTEMA-Nanotechnology Research Group, Mechanical Engineering Department, University of Aveiro, Campus Universitario de Santiago, 3810-193 Aveiro, Portugal

^dCICECO-Aveiro Institute of Materials, Department of Chemistry, University of Aveiro, Campus Universitario de Santiago, 3810-193 Aveiro, Portugal

^eCESAM & Department of Biology, University of Aveiro, Campus Universitario de Santiago, 3810-193 Aveiro, Portugal

^fiBiMED-Institute of Biomedicine, Department of Medical Sciences, University of Aveiro, Agra do Crasto, 3810-193 Aveiro, Portugal

¹Corresponding authors. E-mail: cims@ua.pt (Carla Santos); ermelinda.macoas@tecnico.ulisboa.pt (Ermelinda Maçôas); paulam@ua.pt (Paula Marques)

Abstract

The major limitation in the development of hybrids based on graphene oxide (GO) and porphyrins is their dispersibility and stability in aqueous systems due to the hydrophobic character induced by porphyrins. Most of the previous approaches reported the direct functionalization of GO with polyethylene glycol (PEG) chains followed by the self-assembly of porphyrins by π - π interactions. Here, new hybrids were prepared using porphyrins previously functionalized with different number/types of glycol branches to be covalently attached through esterification to the carboxyl groups of GO sheets of nanometric dimensions. The number of the glycol chains and its relative position in the porphyrin core showed to be fundamental to improve the hybrids dispersion and stability in aqueous solutions. The best performing hybrids were characterized by transmission electron microscopy, X-ray photoelectron spectroscopy, Fourier transform infrared, UV-Vis absorption and fluorescence spectroscopy. The *in vitro* biocompatibility assessment of these hybrids was conducted using human Saos-2 cells. Their effects on cell proliferation and viability, the generation of reactive oxygen species as well as the cell morphology after cell uptake were analyzed. The results demonstrate the biocompatibility of these hybrid nanomaterials with human Saos-2 cells, which is very promising for future application in biomedicine namely in cancer therapy.

1. Introduction

Nano-graphene oxide (nano-GO) is a graphene derivative with nanometric dimensions (<100 nm) [1], and in general, it is obtained by a controlled fragmentation of graphene oxide (GO) promoted by ultrasonication [2]. This carbon nanomaterial has been explored for applications in a large variety of fields including catalysis [3], nanoelectronic devices [4], nanocomposite materials [5], energy devices [6] and nanomedicine [7]. The chemical versatility of nano-GO confers a large potential for the establishment of covalent bonds with other molecules with high relevance for biological applications [8]. In the tailoring of GO for cancer therapy, several surface coating strategies have been reported in the literature over the last few years, such as covalent and non-covalent approaches [9-11], with polymers, biomolecules and nanoparticles for the development of innovative nanoplatforms able to provide, new cancer targeting strategies [12], controlled drug delivery systems [13-14], phototherapies triggered by external stimulus [15-16] and more efficient biomedical imaging probes [17-18].

Polyethylene glycol (PEG) is an example of a hydrophilic biocompatible polymer which has been extensively applied to functionalize nano-GO. It has been shown that PEGylation of GO with branched PEG improved GO stability and its dispersibility in aqueous solutions [19-20]. For instance, Liu and co-workers [21] functionalized nano-GO with PEG and grafted poly(maleic anhydride-alt-1-octadecene) yielding nanoGO-PEG with excellent physiological stability and ultra-long blood circulation half-life, useful to perform cancer photothermal treatment (PTT). Recently, we reported that the PEGylated nano-GO cell internalization mechanism, concentration and kinetic uptake were dependent on the characteristic of each cell type [22]. Furthermore, it was also described that the number of PEG branches has a strong influence on cell viability and cell uptake kinetics [23].

The functionalization of GO with tetrapyrrolic macrocycles, such as phthalocyanines, chlorins and porphyrins is also deserving some attention from the scientific community. These molecules are well-known by their role as photosensitizers (PS) in photodynamic therapy (PDT) an emerging therapeutic modality that has been successful used in the treatment of neoplastic and non-malignant diseases [24]. Part of PDT success rely on the photophysical properties of these macrocycles like high molar absorption coefficient in the visible spectral region, high intersystem-crossing yield, long-lived triplet excited state and low cytotoxicity in dark [25]. The development of porphyrin/GO hybrid materials for cancer therapy and bioimaging is a recent topic of research. From the best of our knowledge the first report for the synthesis of hybrid GO with porphyrins [e.g. 5-(4-aminophenyl)-10,15,20-triphenylporphyrin (NH₂-TPP)] dates from 2009 [26]. The authors observed that the photoinduced electron- and/or energy-transfer mechanisms played a significant role in the superior optical limiting performance of the NH₂-TPP/GO hybrid material. However, it was reported that this graphene hybrid materials just formed stable dispersions in organic solvents. Wang et al. recently reported similar findings on the preparation of covalent bonded porphyrin-reduced graphene oxide (rGO) hybrids via two different strategies using 1,3-dipolar cycloaddition reactions [27]. Suet *al.* proposed the development of new targeted porphyrin/GO hybrids by non-covalent functionalization for brain cancer therapy with good stability in aqueous solutions. They report a higher photothermal conversion when irradiated with 808 nm laser light when compared with graphene counterparts, able to cause significant ablation for *in vitro* brain cancer cells [28]. In another work it was reported the assembly of the cationic porphyrin derivative 5-(p-(4-trimethylammonium)-butoxyphenyl)-10,15,20-triphenylporphyrin bromide (MitoTPP) onto the PEG-functionalized and folic acid-modified nano-GO [29]. The results showed that this dual target nanosystem was

able to release its cargo MitoTPP at lower pH, which subsequently accumulates in mitochondria of cancer cells over expressed with folate receptor (FR). After irradiation with 650 nm light singlet oxygen was generated causing oxidant damage and promoting higher cellular cytotoxicity on those FR-positive cells. Graphene quantum dots (GQDs) produced from hydrothermal treatment of GO were also recently used as a platform for the development of multifunctional theranostic agents [30]. The conjugation of porphyrins into PEGylated and aptamer functionalized GQDs enabled the specific labelling of A549 lung cancer cells that could be detected by *in vitro* bioimaging due to the intrinsic blue fluorescence of GQDs. Moreover, an excellent PTT/PDT therapeutic efficiency was observed for both *in vitro* A549 cancer cells and *in vivo* multicellular tumour spheroids (MCTS) with laser light irradiation at 635/980nm.

The preparation of new hybrids based on porphyrins and nano-GO remains a great challenge to obtain key materials that can fulfil all the biological requirements such as aqueous dispersibility and stability during acceptable periods of time. Herein, we report, for the first time, the synthetic access and full characterization of nano-GO covalently linked to porphyrins bearing glycol branches. Additionally, taking into account the potential biomedical applications of these graphene-based hybrid nanomaterials, their *in vitro* biocompatibility with human Saos-2 osteoblasts was studied.

2. Experimental Section

2.1. Chemicals

Pyrrrole, 2,3,4,5,6-pentafluorobenzaldehyde, nitrobenzene, chloroacetic acid, sodium hydroxide, synthetic graphite flakes and all oxidizing and reducing agents were purchased from Sigma–Aldrich. Ethylene glycol and tetraethylene glycol were obtained from Alfa Aesar. All these

chemicals were used without further purification. The solvents were obtained from Panreac and Riedel-de Haen and used as received or distilled and dried using standard procedures.

2.2. Samples preparation

2.2.1. Synthesis of nano-GO

GO was obtained from exfoliation of high purity graphite in acidic medium by a modified Hummers method [31]. Briefly, a mixture of 2.5 g of graphite, 1.9 g of NaNO_3 and 85 mL of H_2SO_4 was placed in a flask cooled in an ice bath, and the mixture was kept stirring until total homogenization. After that, 11.25 g of KMnO_4 was gradually added to the solution while stirring. After 2 h, the solution was removed from the ice bath, and further stirred for 5 days. Finally, a brown-coloured viscous slurry was obtained. The mixture was washed with an aqueous solution (500 mL) of 3 wt % H_2SO_4 and 0.5 wt % H_2O_2 . The solid product obtained after the rigorous cleaning process was rinsed using copious amounts of distilled water. Finally, the resulting GO was dried by lyophilisation in order to obtain a non-agglomerated dried powder.

The nano-GO preparation was based on the breakage of GO by combined mechanical aging and tip sonication processes [4]. Briefly, GO was re-suspended in water with a concentration of 1 mg/mL and subjected to ultra-sonication treatment (Vibra Cell Bioblock Scientific model 75,043 at 225 W) during 3 hours at room temperature.

2.2.2. Functionalization of nano-GO with extra carboxylic groups (nanoGO-CO₂H)

The nano-GO obtained by ultrasonic treatment with an average lateral size of *ca* 50 nm was further functionalized with carboxylic groups to improve its capability to be esterified with the porphyrins bearing glycol units. For that purpose, a nano-GO dispersion in NaOH (1.25 M) was

prepared (1 mg/mL). The carboxylic groups were activated by adding 2.5 g of chloroacetic acid to 50 mL of the dispersion and the reaction mixture was maintained in an ultrasonication bath (Bandelin SONOREX Digital 10P) for 180 min at 25 °C. The resulting nanoGO-CO₂H dispersion with extra carboxylic groups was neutralized and purified by repeated rinsing and filtrations (further details in Supporting Information- Figures S1 and S2) [32]. For simplicity this sample will be just labelled as nanoGO-CO₂H.

2.2.3. *Synthesis of glycol porphyrins*

The synthetic access to the template 5,10,15,20-tetrakis(pentafluorophenyl)porphyrin (**P1**) and to porphyrins **P2-4** bearing ethylene glycol chains (see structures in Figure 1) followed experimental procedures described in the literature [33]. An extension of that protocol to tetraethylene glycol allowed to obtain porphyrins **P5-7** with a longer glycol chain.

2.2.4. *Synthesis of porphyrins P5-7*

A flask under an inert atmosphere (Ar) was charged with sodium hydride (15 mg, 0.66 mmol), tetraethylene glycol (12.5 mmol) and tetrahydrofuran (15 mL). The mixture was refluxed for 30 min. Then, 5,10,15,20-tetrakis(pentafluorophenyl)porphyrin (75 mg, 0.076 mmol) and tetrahydrofuran (15 mL) were added and the resulting reaction mixture was maintained under reflux for 8 h. After cooling to room temperature, the mixture was diluted with chloroform and washed three times with water. The organic solvent was evaporated and the crude was purified on silica gel preparative TLC plates using as eluent a mixture of chloroform-methanol (9:1). Porphyrins **P5-7** were obtained pure after crystallization in chloroform:methanol. The structures

of the derivatives **P5-7** were established by spectroscopic data, namely ^1H and ^{19}F NMR, UV-Vis and MS (Figures S4-S7, Supporting Information).

Porphyrin 5 (P5 opp): RMN ^1H (CDCl_3), δ (ppm) and J (Hz):- 2.91 (broad s, 2H, NH), 3.65-3.62 (m, 6H, CH_2), 3.77-3.76 (m, 12H, CH_2 and OH), 3.83-3.81 (m, 4H, CH_2), 3.89-3.87 (m, 4H, CH_2), 4.09 (t, $J = 4.4$ Hz, 4H, CH_2), 4.78 (t, $J = 4.4$ Hz, 4H, CH_2), 8.90 (d, $J = 4.8$ Hz, 4H, H- β), 8.96 (d, $J = 4.8$ Hz, 4H, H- β).

^{19}F NMR (CDCl_3): -159.55 (dd, $J = 25.5, 7.5$ Hz, 4F, *Forto*), -161.93 (dd, $J = 24.0, 9.0$ Hz, 4F, *Forto*), -174.54 (t, $J = 21.0$ Hz, 2F, *Fpara*), -179.91 (dd, $J = 25.5, 7.5$ Hz, 4F, *Fmeta*), -184.50 (dt, $J = 24.0, 9.0$ Hz, 4F, *Fmeta*).

HRMS-ESI: $[\text{M}+2\text{H}]^{2+}$ (calculated for $\text{C}_{60}\text{H}_{46}\text{F}_{18}\text{N}_4\text{O}_{10}$) m/z 663.13362

Yield:24%

Porphyrin 5 (P5 adj): RMN ^1H (CDCl_3), δ (ppm) and J (Hz): - 2.91 (broad s, 2H, NH), 3.65-3.62 (m, 4H, CH_2), 3.77-3.74 (m, 14 H, CH_2 and OH), 3.82-3.79 (m, 4H, CH_2), 3.90-3.86 (m, 4H, CH_2), 4.09 (t, $J = 4.4$ Hz, 4H, CH_2), 4.78 (t, $J = 4.4$ Hz, 4H, CH_2), 8.90 (d, $J = 4.5$ Hz, 4H, H- β), 8.97 (d, $J = 4.5$ Hz, 4H, H- β).

^{19}F NMR (CDCl_3): -159.53 (dd, $J = 24.0, 9.0$ Hz, 4F, *Forto*), -161.38 (dd, $J = 22.5, 7.5$ Hz, 4F, *Forto*), -174.36 (t, $J = 22.5$ Hz, 2F, *Fpara*), -180.08 (dd, $J = 24.0, 9.0$ Hz, 4F, *Fmeta*), -184.45 (dt, $J = 22.5, 7.5$ Hz, 4F, *Fmeta*).

HRMS-ESI: $[\text{M}+2\text{H}]^{2+}$ (calculated for $\text{C}_{60}\text{H}_{46}\text{F}_{18}\text{N}_4\text{O}_{10}$) m/z 663.13257

Yield: 11%

Porphyrin 6 (P6): RMN ^1H (CDCl_3), δ (ppm) and J (Hz): - 2.90 (broad s, 2H, NH), 3.64-3.62 (m, 6 H, CH_2), 3.81-3.79 (m, 20 H, CH_2 and OH), 3.89-3.87 (m, 6H, CH_2), 3.89-3.86 (m, 6H,

CH₂), 4.08 (t, $J = 4.4$ Hz, 6H, CH₂), 4.77 (t, $J = 4.4$ Hz, 6H, CH₂), 8.89 (d, $J = 4.0$ Hz, 2H, H- β), 8.96 (broad s, 6H, H- β).

¹⁹F NMR (CDCl₃): -159.54 (dd, $J = 24.0, 9.0$ Hz, 2F, *Forto*), -161.94 (dd, $J = 22.5, 7.5$ Hz, 6F, *Forto*), -174.67 (t, $J = 22.5$ Hz, 1F, *Fpara*), -179.97 (dd, $J = 22.5, 7.5$ Hz, 6F, *Fmeta*), -184.58 to -184.72 (m, 2F, *Fmeta*).

Porphyrin 7 (P7): RMN ¹H (CDCl₃), δ (ppm) and J (Hz): - 2.89 (broad s, 2H, NH), 3.66-3.63 (m, 8H, CH₂), 3.76-3.74 (m, 28 H, CH₂ and OH), 3.79-3.77 (m, 8H, CH₂), 3.87-3.85 (m, 8H, CH₂), 4.06 (t, $J = 4.4$ Hz, 8H, CH₂), 4.76 (t, $J = 4.4$ Hz, 8H, CH₂), 8.95 (broad s, 8 H, H- β). ¹⁹F NMR (CDCl₃): -161.93 (dd, $J = 24.0, 9.0$ Hz, 8F,*Forto*); -180.01 (dd, $J = 24.0, 9.0$ Hz, 8F, *Fmeta*).

HRMS-ESI: [M+2H]²⁺ (calculated for C₇₆H₈₀F₁₆N₄O₂₀) m/z 836.25497.

Yield:18%

2.2.5. Functionalization of nanoGO-CO₂H with glycol porphyrins

The functionalization of the nanoGO-CO₂H with porphyrins **P2-P7** via ester linkages was performed using EDAC [1-ethyl-3-(3-dimethylaminopropyl) carbodiimide hydrochloride] to activate the carboxyl groups. Before the coupling, 0.04 g of EDAC was added to 45 mL of nanoGO-CO₂H aqueous solution (1 mg/mL) and the resulting mixture was maintained under vigorous stirring for 3 h. Then, the glycol porphyrins **P2-P7** (*ca* 20 mg) dissolved in tetrahydrofuran (15 mL) were added and the resulting reaction mixture was maintained under stirring for 48 h at room temperature. The solid product obtained was filtered and washed with THF, until no sign of porphyrin was found in the UV-Vis absorption and emission spectra (excitation of the Soret band at 411 nm) of the waste solution. The different nano-GO/porphyrin

hybrids were labelled as nanoGO-Px where X is the number used in Figure 1 to identify each porphyrin.

2.3. Materials Characterization

Elemental analyses were carried out with a Fisons Instruments EA1108 microanalyser at the University of Vigo (CACTI), Spain. ^1H and ^{13}C NMR spectra were recorded on Bruker Avance 300 (at 300 and 75 MHz, respectively) spectrometers. ^{19}F NMR spectra were also obtained on a Bruker Avance 300 at 282 MHz. CDCl_3 was used as solvent with tetramethylsilane (TMS) as the internal reference; the chemical shifts are expressed in δ (ppm) with the coupling constants (J) in Hertz (Hz). Unequivocal ^1H assignments were made using 2D COSY experiments (mixing time of 800 ms). Preparative thin-layer chromatography (TLC) was carried out on 20×20 cm glass plates coated with silica gel (0.5 mm thick). Analytical TLC was carried out on pre-coated sheets with silica gel (Merck 60, 0.2 mm thick).

Transmission electron microscopy (TEM) was performed using a Hitachi H-9000 operating at 300KV. The samples for TEM were prepared by depositing aliquots of the corresponding dispersion onto a carbon-coated copper grid and then letting the solvent evaporate.

The FTIR spectra of different samples were recorded with a Mattson 7000 FT-IR spectrometer (8 cm^{-1} resolution and 256 interferograms) using KBr pellets (Aldrich, 99%, FT-IR grade).

XPS spectra were acquired in an Ultra High Vacuum (UHV) system with a base pressure of 2×10^{-10} mbar. The system is equipped with a hemispherical electron energy analyser (SPECS Phoibos 150), a delay-line detector and a monochromatic $\text{AlK}\alpha$ (1486.74 eV) X-ray source. High resolution spectra were recorded at normal emission take-off angle with a pass-energy of 20 eV for C1s, N1s and F1s spectra.

Micro-Raman experiments were performed at room temperature using the 488 nm Ar-ion laser with an incident power of 1 mW. The light was focused and collected with an Olympus microscope (320 objective) and a “super-notch-plus” filter from Kaiser was used to eliminate elastic light. The scattered light was analysed with a Jobin -Yvon HR-460 monochromator coupled to a Peltier cooled CCD.

Thermal gravimetric analyses were performed using a Pyris 6, Perkin-Elmet from 25 °C to 800 °C with a scan rate of 10 °C min⁻¹. Samples (1 to 2 mg) were weighed into a ceramic crucible.

Absorption spectra were recorded on a JASCO V-650 spectrophotometer. The fluorescence emission spectra were measured either in a Fluoromax-4 or a Fluorolog-3 (Horiba). The emission spectra were corrected for the optical response of the monochromator-detector system and the excitation spectra were corrected for the spectral distribution of the lamp intensity using a photodiode reference detector. Solutions of 0.2 mg/mL of nanoGO-PX were used in the optical characterization corresponding to a concentration of porphyrin of the order of 1x10⁻⁶ M. This concentration was estimated from the absorption spectra of 0.2 mg/mL solutions of the nanoGO-PX hybrids in mixtures of water and good solvents using the absorption coefficient of the isolated porphyrins in good solvents. Solutions of 10⁻⁶ M concentration were also used in the optical characterization of the isolated porphyrins.

2.4. Biological Assays

2.4.1. Proliferation and viability of human sarcoma osteoblasts

The biocompatibility of the hybrid nanomaterials was investigated considering the proliferation and the viability assays carried out with human Saos-2 osteoblasts, as an osteosarcoma cell line.

This particular type of cell line was chosen due to the popularity of such model cells in the evaluation of biocompatibility and cytotoxicity of graphene-related nanomaterials [23, 34-36], and the challenge that the treatment of deep tumors such as osteosarcoma represent to photodynamic therapy [37].

The cells were seeded onto 6-well plates at a density of 200,000 cells/mL in Dulbecco's Modified Eagle Medium (DMEM), supplemented with 10% fetal bovine serum (FBS; Gibco BRL), 1 mM L-glutamine (BioWhittaker Europe), penicillin (800 µg/mL; BioWhittaker Europe) and streptomycin (800 µg/mL; BioWhittaker Europe) under CO₂ (5%) in a humidified atmosphere at 37 °C for 24 h. Subsequently, the culture medium was replaced by a fresh one, to which an aqueous dispersion of hybrid nanomaterials was added to reach a final concentration in the medium of 50 µg/mL (with 2-3 min of bath sonication to homogenize the mixture).

Then, the cell population with the material-containing culture medium was kept under a CO₂ (5%) in a humidified atmosphere at 37 °C for 24 h before carrying out the cell assays. Samples corresponding to cells cultured in the absence of material (Ctrl) and in the presence of 50 µg/mL of nanoGO-CO₂H were always included in the assays as control cells and starting material, respectively. The Saos-2 osteoblasts were cultured in the presence of 50 µg/mL of nanoGO-P2 or of nanoGO-P5, the most promising hybrids in terms of aqueous stability and will be referred as **P2** and **P5** conditions, respectively.

The dye exclusion test (trypan blue) was used to estimate the cell viability and proliferation. Trypan blue is a vital stain that is not absorbed by healthy viable cells. When cells are damaged or dead, trypan blue can enter the cell, allowing dead cells to be counted. Cells exposed to 1% Triton X-100 for 10 min were used as positive controls for cell death. After 24 h of culture in the presence of the hybrid materials, the cells were washed repeatedly with phosphate-buffered

saline (PBS) and incubated with 0.25% trypsin-EDTA for 10 min in 5% CO₂ atmosphere at 37 °C to detach them. Then, the cells were re-suspended in fresh culture medium and analyzed with the viability analyser (Vi-CELL™RX, Beckman Coulter).

2.4.2. Reactive Oxygen Species (ROS) Quantification by Flow Cytometry

ROS generation was assayed by flow cytometry (FCM) using the fluorescent probe 2,7-dichlorodihydrofluorescein diacetate (DCFDA) (Sigma-Aldrich, St. Louis, MO-USA), which upon acetate cleavage is oxidized to fluorescent dichlorofluorescein (DCF) by ROS. Cells exposed to 140 µM H₂O₂ for 24 h at 37°C were used as positive controls for the presence of ROS. After the exposure period to the hybrid nanomaterials, the cell culture was gently washed with PBS to eliminate the unincorporated nanomaterial and cells were incubated with the DCFDA probe for 45 min at 37°C. The DCFDA probe is not fluorescent, but in the presence of ROS it is oxidized and emits green fluorescence that can be detected at 525 nm upon excitation at 488 nm. After the incubation time with the probe, the cells were re-washed with PBS to eliminate excess probe, incubated with trypsin-EDTA and resuspended in a new culture medium at 4°C and supplemented with 2% FBS. These conditions of the culture medium help to keep the cell culture metabolically stopped, thus avoiding the production of ROS associated to the procedure and not to the nanomaterial itself (false positive data). Cells were analysed in a Coulter EPICS XL flow cytometer and ROS formation was estimated by the mean fluorescence intensity parameter using the FlowJo software (Tree Star Inc., Ashland, OR-USA).

2.4.3. Cell uptake potential by flow cytometry light scattering analysis

For cell uptake assays, Saos-2 cells were allowed to attach in 6-well plates under cell culture conditions for 24 h. After this time, the different hybrid nanomaterials were incorporated to the cell cultures and cells were incubated during 24 hours. Subsequently, cells were washed with PBS, trypsinized and suspended in fresh cell culture medium (DMEM).

The amount of hybrid nanomaterials taken up by Saos-2 cells was evaluated using a flow cytometric light scattering analyser [38-39]. In flow cytometry, the light detected at a scatter angle of 90° is called side-scatter (SSC) light, and the SSC intensity is proportional to the intracellular complexity. This property is determined in part by cell cytoplasm, mitochondria and pinocytotic vesicles [40]. The laser light collected at small scatter angles is called forward-scatter (FSC) light, and the FSC intensity is proportional to the cell size. In this study we performed a quantitative evaluation of the uptake of graphene-based nanomaterials into human Saos-2 cells by evaluating the shift in the flow cytometric side scatter in a similar approach as followed by others [36]. To further confirm the incorporation of the nanomaterial and distinguish from possible simple adhesion to the outer cell membrane, some additional experiments have been performed where the endocytosis was inhibited in one set of samples by cell incubation with the nanomaterials at 4°C for 4h [39], while another set was normally incubated at 37°C . A clear shift was observed in the flow cytometric side scatter of the cells incubated at 37°C comparatively to those exposed at 4°C , proving intracellular agglomeration the nanomaterials in the former (See Supporting Information-Figure S8). The SSC and FSC light were measured in a Coulter XL Flow Cytometer (Beckman Coulter, Hialeah, FL-USA) equipped with an argon ion laser (15 mW, 488 nm). Acquisitions were made using SYSTEM II software v. 3.0 (Beckman Coulter, Hialeah, FL). For each sample, 10000 - 60000 cells were analysed at a flow rate of about 1000 cells/s.

2.4.4. Confocal microscopy studies

Human Saos-2 osteoblasts were grown on glass coverslips and cultured in the presence of 50 $\mu\text{g}/\text{mL}$ hybrid nanomaterials dispersed in culture medium for 24 hours. Cells were fixed with a 4% paraformaldehyde in PBS for 30 min, permeabilized with a 0.2% Triton X-100/PBS solution and blocked with 3% BSA in PBS for 1 hour. For immunocytochemistry procedures, cells were incubated for 2 hours with primary antibodies - rabbit anti-type-I collagen I (Novus Biologicals), and mouse anti-acetylated- α -tubulin (Sigma-Aldrich) - followed by 1 hour incubation with green fluorescing Alexa Fluor 488-linked secondary antibodies (Molecular Probes). Alternatively, cells were directly labelled with Alexa Fluor 488-labelled Phalloidin (Abcam) to stain filamentous actin. Following washes with PBS and deionised water, coverslips were mounted onto glass slides with 4',6-diamidino-2-phenylindole (DAPI)-containing Vectashield mounting medium (Vector Labs). Microphotographs were acquired on a LSM 510 META confocal microscope (Zeiss, Jena, Germany) through a Plan-Neofluor 63x/1.4 oil immersion objective. DAPI fluorescence was collected at 420-480 nm ($\lambda_{\text{exc}} = 405$ nm), Alexa488 fluorescence at 505-565 nm, and porphyrin fluorescence at 650-754 nm ($\lambda_{\text{exc}} = 405$ nm).

2.4.5. Statistical analysis

The cell assay data were expressed as a mean \pm standard deviation of a representative of four independent experiments carried out in triplicate. Statistical analysis was performed using the Statistical Package for the Social Sciences (SPSS) software (version 19). Statistical comparisons were made by analysis of variance (ANOVA). The Scheffé test was used for *post hoc*

evaluations of differences among groups. In the statistical evaluations, $p < 0.05$ was considered as statistically significant.

3. Results and Discussion

3.1. Covalent functionalization of NanoGO-CO₂H with glycol porphyrins

Two series of porphyrins bearing two (**P2opp**, **P2adj**, **P5opp**, **P5adj**), three (**P3** and **P6**) and four (**P4** and **P7**) glycol branches were prepared (Figure 1). Porphyrins **P2-P4** with shorter chains were obtained by a step-wise nucleophilic substitution of the para fluorine atom of 5,10,15,20-tetrakis(pentafluorophenyl)porphyrin (**P1**, Figure 1) with ethylene glycol [33]. The extension of this strategy to tetraethylene glycol afforded the other series of porphyrins **P5-P7** with longer chains.

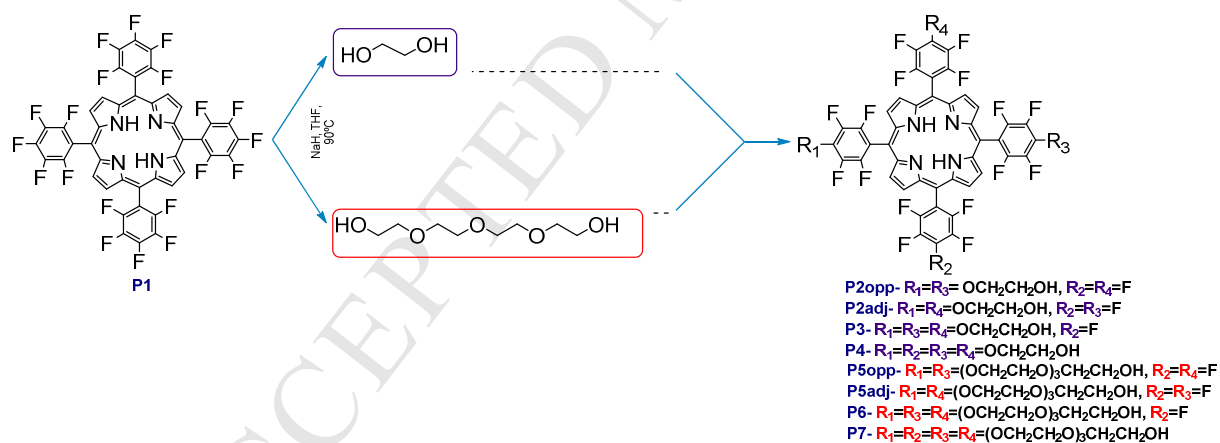


Figure 1. Structure of the template 5, 10, 15, 20-tetrakis(pentafluorophenyl)porphyrin and of the glycol porphyrins **P2-P7**

The incorporation of porphyrins isolated in better yields, **P2opp**, **P3,P4**, **P5opp**, **P6** and **P7** through an ester bond on the nanoGO-CO₂H was successfully achieved using EDAC to activate the carboxyl groups present in the nano-GO as exemplified in Figure 2 for porphyrins **P2opp** and **P5opp**. After the coupling reactions the resulting solids were filtered and thoroughly washed with adequate solvents to remove any unreacted porphyrin. The *as*-prepared nanoGO-porphyrin hybrids are labeled as nanoGO-PX where X is the number of the porphyrin (Figure 1). No attempts were performed to incorporate **P2adj** and **P5adj** in to nanoGO-CO₂H due to the lower yields obtained during their synthesis; thus, porphyrins **P2opp** and **P5opp** in nanoGO-PX will be just labelled as **P2** and **P5**.

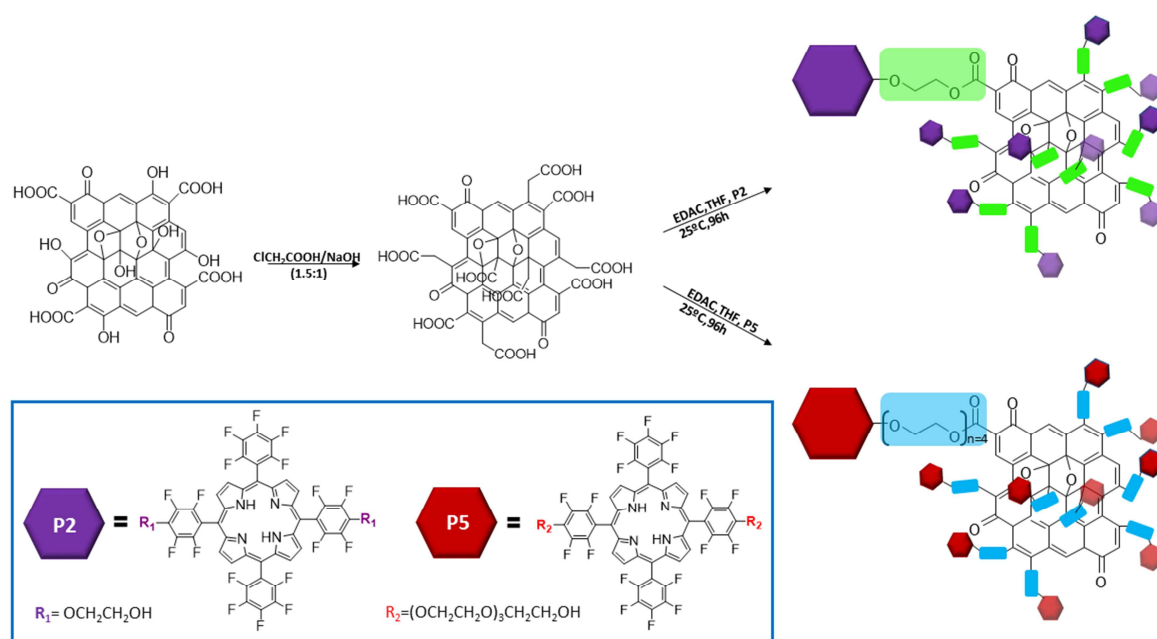


Figure 2. Illustration of the synthetic route used to functionalize covalently nanoGO-CO₂H with porphyrin **P2** and **P5** bearing two glycol units in opposite pentafluorophenyl groups using the activating agent EDAC.

Figure 3 shows the hydrodynamic radius of the nano-GO hybrids bearing two (di), three (tris) or four (tetra) branches of either ethylene glycol (**P2**, **P3** and **P4**) or tetraethylene glycol (**P5**, **P6** and **P7**) substituted porphyrins. For both series, the hydrodynamic radius is relatively insensitive to the size of the glycol chain and quite sensitive to the number of branches in the porphyrins. A linear increase of the nanoGO-CO₂H hydrodynamic radius is observed with the number of branches in the porphyrins. The radius increases from the initial radius of 50 nm of nanoGO-CO₂H to 170-190 nm for the di-substituted porphyrins (nanoGO-**P2** and -**P5**), 225-300 nm for the tri-substituted porphyrins (nanoGO-**P3** and -**P6**) and finally 240-310 nm for the tetra-substituted porphyrins (nanoGO-**P4** and nanoGO-**P7**) (Figure 3). The increase in the size of the hybrids with the number of branches in the porphyrin suggests that the porphyrins act as a bridge between different nano-GO sheets.

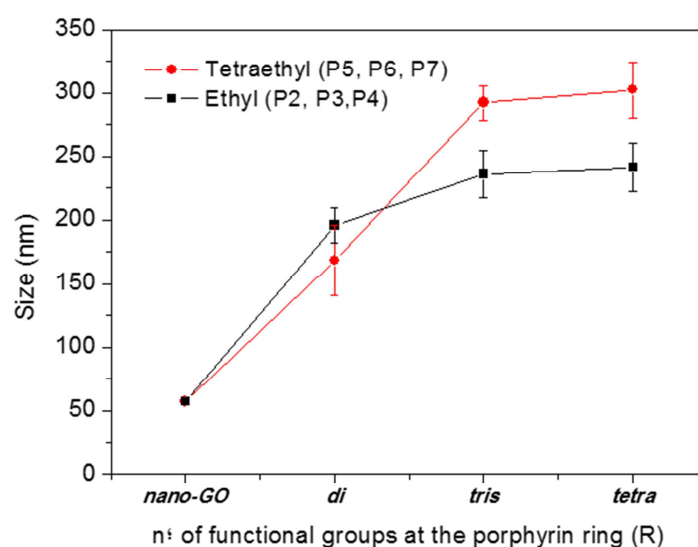


Figure 3. Hydrodynamic radius of the nano-GO and nano-GO functionalized with porphyrins of both series bearing two (di), three (tris) or four (tetra) branches of glycol units.

It is worth to refer that the aqueous dispersions of the hybrids bearing porphyrins with two glycol branches in opposite position (nanoGO-**P2** and nanoGO-**P5**) show a better long term stability than the other hybrids with more branched porphyrins. The presence of more glycol chains was expected to increase the porphyrin solubility; however a higher number of chains seems to have the adverse effect of promoting aggregation in the hybrids. This trend is probably due to the bridging effect brought by the hydrogen bonding involving the OH groups at the glycol chains ends. The intermolecular hydrogen bonding may involve the glycol chains of two different hybrids or the glycol chain of one hybrid and the OH groups in the basal plane of the nano-GO in another hybrid. In any case, increasing the number of glycol chains increases the probability of inter-hybrid hydrogen bonding, thus promoting aggregation. Considering the higher stability of the hybrids bearing di-substituted porphyrins we focus in the physicochemical characterization of the hybrids nanoGO-**P2** and nanoGO-**P5**.

3.2. *Characterization of the nanoGO-Px hybrids*

The covalent functionalization of nanoGO-CO₂H with the glycol porphyrins **P2** and **P5** was confirmed and supported from FTIR analysis. Figure 4 shows, as an example, the FTIR spectra of nanoGO-CO₂H, porphyrin **P5** and nanoGO-**P5**. The absorption peaks of nanoGO-CO₂H are those characteristic of protonated carboxylic acid/carboxylates and condensed aromatic rings. The carbonyl stretching mode of protonated carboxylic acids appears quite isolated at (1731 cm⁻¹). The band at 1620 cm⁻¹ can have contributions from both the symmetric O-C-O stretching of carboxylates and the C=C stretching of aromatic ring [41-43]. The asymmetric O-C-O stretching, the bending modes of carboxylates and the C-OH bending and C-O stretching mode of

protonated carboxylic acids are responsible for the broad bands peaking at 1415 cm^{-1} , 1227 cm^{-1} and 1070 cm^{-1} . The coupling between the different modes within the carboxylic group and the carboxylate group and the heterogeneity of the systems preclude a more detailed assignment of the vibrational modes contributing to each band [44-45]. The spectrum of porphyrin **P5** exhibits the typical FTIR bands of free-base porphyrins at: 3342 , 3122 , and 2937 cm^{-1} , due to NH, CH (phenyl), and CH (pyrrole) stretching, respectively; 1575 cm^{-1} , related to symmetric angular deformation in the plane of the pyrrole ring NH and 1372 cm^{-1} related to C–N axial deformation, among others. In addition, the characteristic bands of the tetraethylene glycol units linked to the porphyrin, can be seen at 1078 cm^{-1} (C–O–C symmetric axial deformation), 1152 cm^{-1} (C–O–C asymmetric axial deformation), 1457 cm^{-1} (CH deformation), and 3434 cm^{-1} (OH stretching) [46]. After the covalent functionalization, the FTIR spectrum of nanoGO-**P5** showed an increased structure in the band of the C=O stretching mode (1730 cm^{-1}) that can be attributed to the presence of new ester groups. The intensity of these structured broad band increases with respect to the band at 1620 cm^{-1} not only due to the formation of new ester groups but also due to a decrease in the intensity of the symmetric OCO stretching associate with a reduction in the number of carboxylate groups.

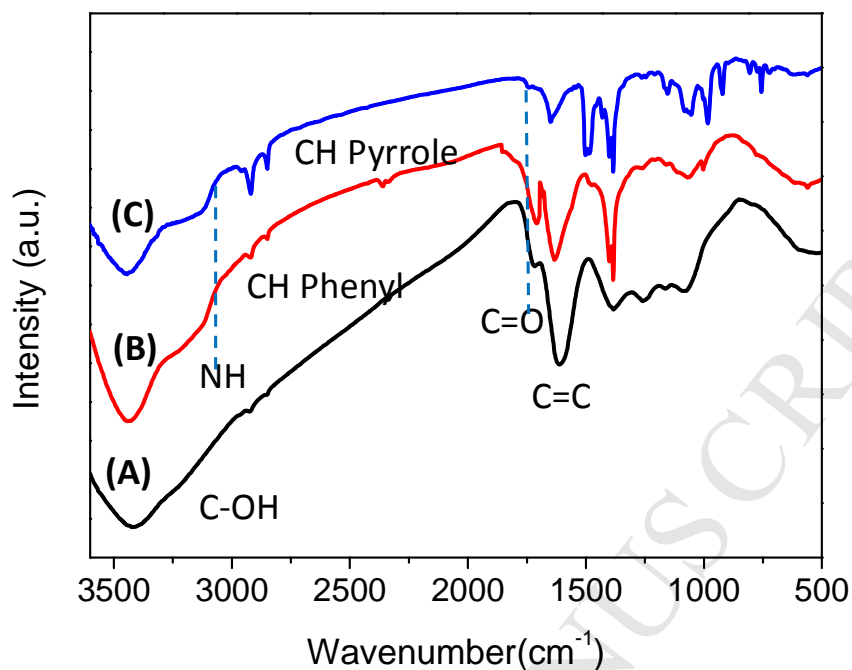


Figure 4. FTIR spectra of nanoGO-CO₂H (A), nanoGO-P5 (B) and porphyrin P5(C).

The FTIR spectrum of the conjugate nanoGO-P2 (Figure S9 in Supporting Information) shows similar features confirming that the glycol porphyrins P2 are covalently linked to the nano-GO sheets through ester bonds.

In Figures 5 and 6 the UV-vis absorption and fluorescence spectra of the nanoGO-porphyrin hybrids are shown in comparison with that of nanoGO-CO₂H and of the isolated porphyrins P2 and P5 in different solvents. The UV-vis absorption spectrum of nanoGO-CO₂H exhibits a broad and unstructured band continuously decreasing from the UV up to the Near-IR in close agreement with the literature [43,47]. The spectroscopic features of both porphyrins in good solvents (THF or DMF) are quite alike but also in agreement with the literature for analogous porphyrins [48-49]. The absorption spectra of the porphyrins contain a strong peak at 411 nm ascribed to the Soret band (Figures 5A and 6A), as well as a group of four weaker bands in the

500-660 nm region attributed to the Q-bands. The hybrids show a combination of the characteristic features of both nanoGO-CO₂H and of the conjugated porphyrins with a clear Soret bands emerging from the unstructured absorption of the nano-GO and a structured absorption also discernible in the Q-band region. For the hybrids in water, the Soret bands appear to be broader and slightly redshifted, whereas the hybrids in DMF show a considerably narrower Soret band with a peak exactly overlapping that of the porphyrins in good solvents (Figures 5A and 6A). These spectral changes in the different solvents could be due to solvatochromic effects, π - π interactions with GO or the formation of porphyrin aggregates [48, 50-51]. To unravel the origin of this effect on the Soret band a careful analysis of the emission and photoexcitation spectra is presented.

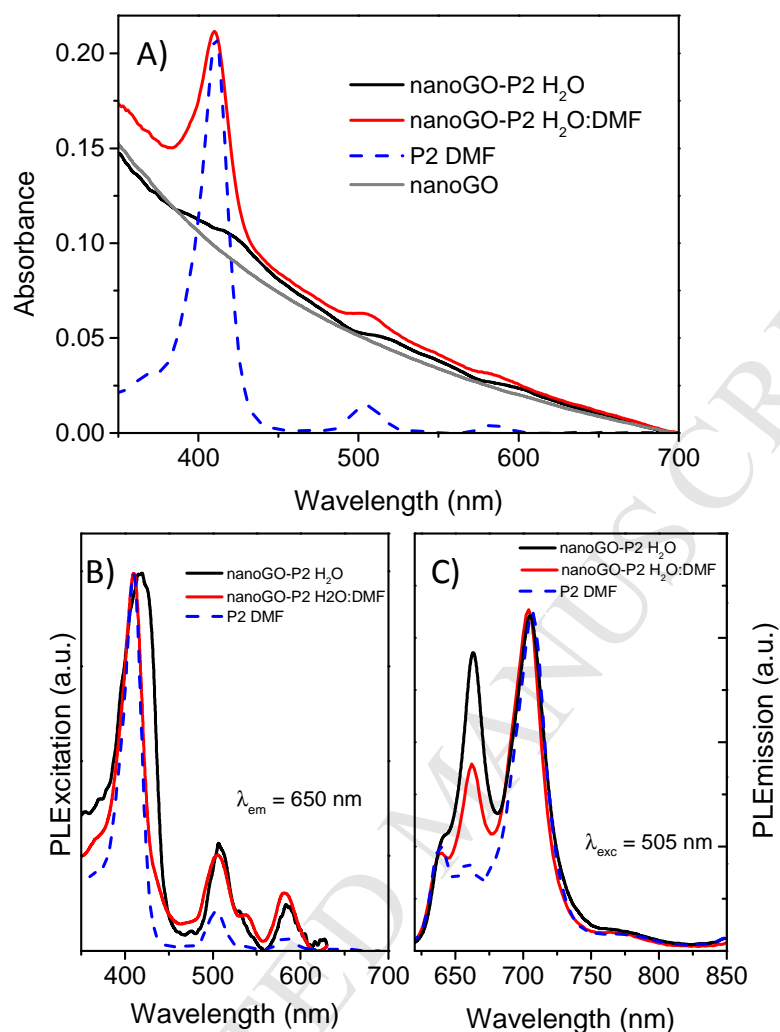


Figure 5. UV-Vis absorption (A), photoexcitation normalized (B) and normalized emission (C) spectra of nanoGO-P2 in H₂O and in 1:1 H₂O:DMF mixture compared with P2 in DMF.

In Figures 5C and 6C, the emission spectra of both porphyrins in DMF collected upon excitation at the strongest Q-band (505 nm) show a typical doublet structure with a stronger Q(0,1) band peaking at c.a. 710 nm and a weaker Q(0,0) band centered at c.a. 650 nm. The emission quantum yields measured in good solvents are about 6%. NanoGO-P2 exhibits an extra sharp emission band at 665 nm assigned to the formation of aggregates (Figure 5C). The

assignment is supported by the fact that the intensity of the peak at 665 nm increases with respect to that of the peak at 750 nm from the H₂O:DMF solvent mixture to pure water. In fact, even in DMF it is possible to see a small peak at 665 nm for **P2** showing that also in such “good” solvent there was a residual amount of aggregates. In Figure 5B, the photoexcitation spectrum of nanoGO-**P2** in water shows a clear red-shift and increased FWHM (full width at half maximum) of the Soret band that supports the formation of J-aggregates [52]. Note that the π - π interaction with the carbon core could also lead to broader and red-shifted Soret bands but it is not expected to result in the formation of new emission bands [43]. As a further support to the formation of porphyrin aggregates, the absorption, emission and photoexcitation spectra of the precursor porphyrin **P1** in water:THF mixtures is shown in Supporting Information illustrating the expected trends upon formation of J-aggregates (Figure S10). The formation of these aggregates does not seem to be dependent upon the concentration of nanoGO-**P2** in solution. It was checked that varying the concentration by two orders of magnitude has no effect on the relative intensity of the bands at 665 nm (J-aggregates) and 710 nm (monomer). Thus, it can be concluded that the aggregates are formed among porphyrins within the same nano-GO sheet.

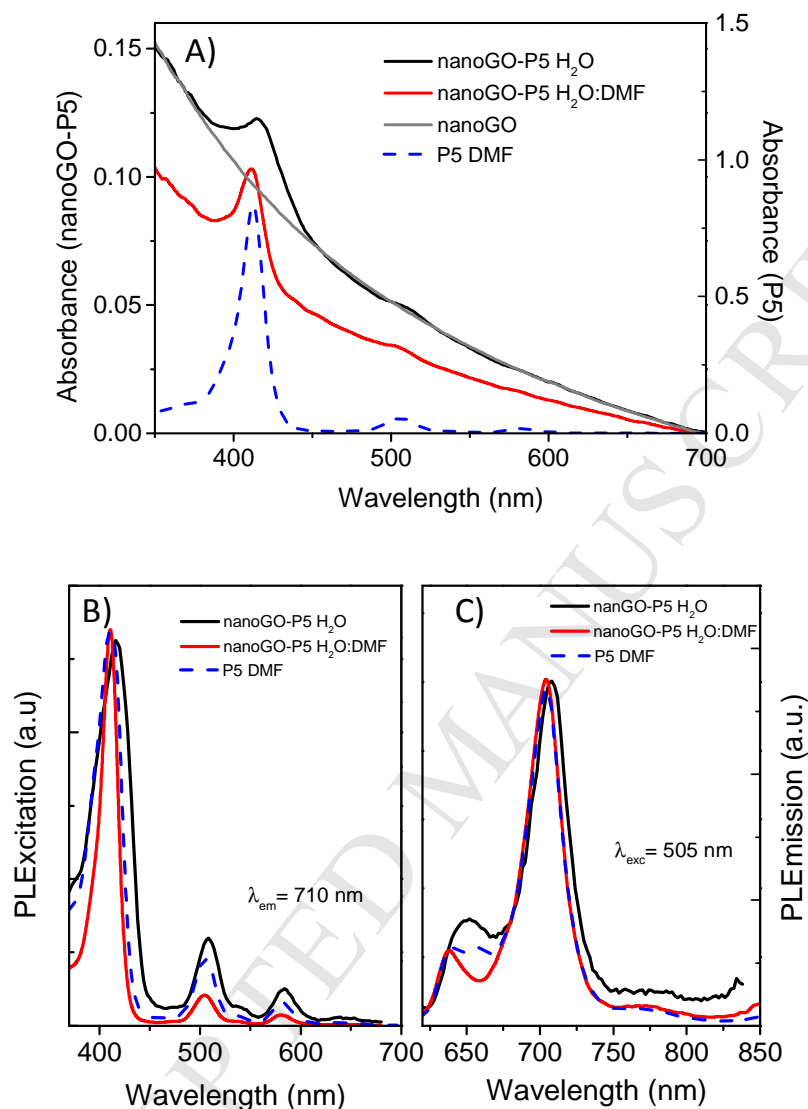


Figure 6. UV-Vis absorption (A), normalized photoexcitation (B) and normalized emission (C) spectra of nanoGO-P5 in H₂O and a 1:1 H₂O:DMF mixture compared with P5 DMF.

For nanoGO-P5 neither in the water:DMF 1:1 mixture nor in water the emission band at 660 nm characteristic of the formation of J-aggregates was observed (Figure 6C). This fact alone would suggest that the longer glycol chain prevents aggregation of the porphyrin. However, P5 alone in DMF:water mixtures will form J-aggregates (see Supporting Information - Figure

S11). Thus, immobilization in nano-GO has proven to be critical to stabilize the porphyrin in water making these hybrids promising materials for biological applications. UV-Vis spectroscopy provides one of the strongest evidence of the fact that the porphyrins are indeed covalently bonded to nano-GO and not just adsorbed on its surface. The absorption spectra of negative control reactions where the functionalization procedure was performed in the absence of EDAC showed no sign of the strong Soret band (Figure S12 in Supporting Information). Moreover, fluorescence spectra, with a limit of detection much lower than electronic absorption, showed no typical emission of porphyrins upon excitation at the wavelength of the Soret band (411 nm) or at one of the Q-band (505 nm).

Further support on the covalent functionalization of the glycol porphyrins **P2** and **P5** to the nanoGO-CO₂H was obtained from Raman. Figure 7A displays the Raman spectra of the nanoGO-CO₂H and of the respective hybrid materials. The characteristic diamondoid (D) and graphitic (G) bands were observed for all samples at around 1387 cm⁻¹ and 1590 cm⁻¹, respectively. The marginal increase on the D to G band intensity ratio (I_D/I_G), from 1.60 in nanoGO-CO₂H to 1.63 in nanoGO-**P2** and 1.66 in nanoGO-**P5** shows that the covalent modification of nano-GO does not introduce a significant additional disorder in the graphene core of the nano-hybrids [53-56]. This is the expected trend since the porphyrins will attach to nanoGO-CO₂H via pre-existent defects, the carboxylic groups. It is worth noting that the physical adsorption of porphyrins to the nano-GO via π - π stacking interaction can lead to very substantial variation of the I_D/I_G intensity ratio. Thus, the modest change of the I_D/I_G intensity ratio observed upon conjugation tells us that the physical adsorption of the porphyrin onto the nano-GO sp² core is not taking place. This lack of non-covalent interaction between the porphyrins and the nano-GO was further supported by invariance of the absorption and emission

spectra of the porphyrin in a 40:60 water:THF dispersion containing increasing amounts of nano-GO (up to 0.33 mg/mL, Figure S13 in Supporting Information).

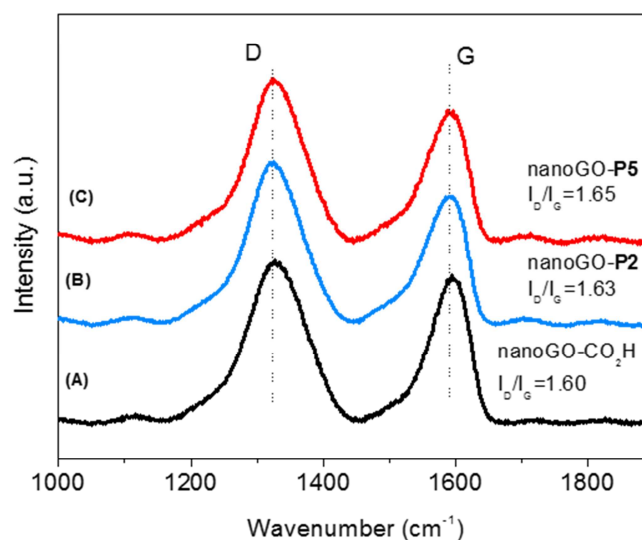


Figure 7. Raman Spectra of nanoGO-CO₂H (A), nanoGO-P2 (B) and nanoGO-P5 (C).

In order to have a better description of the nano-conjugates, the chemical composition of GO, nanoGO-CO₂H, nanoGO-P2, nanoGO-P5 and of porphyrin P2 were investigated by XPS analysis (Figure 8, and Figure S14). The content of epoxy groups and hydroxyl groups decrease from GO to nanoGO-CO₂H due to the combined effect of a well-documented reduction of the GO during its breakdown into the nanoscale [4] and the conversion of such groups in carboxylic groups during the subsequent carboxylation process [43]. For hybrids nanoGO-P2 and nanoGO-P5 evidences of a successful functionalization can be observed by the appearance of N 1s and F 1s peaks located at *ca* 399.3 eV, 400.2 eV and 690 eV, respectively (Figure 8). The deconvoluted N 1s region for nanoGO-P2 exhibits two peaks at 400.0 and 403.2 eV attributed to N-H and C=N present in the porphyrin core, respectively [57]. A similar behavior

was observed for nanoGO-**P5**, where the binding energies of the N 1s region are centered at 401.0 (N-H) and 403.8 eV (C=N).

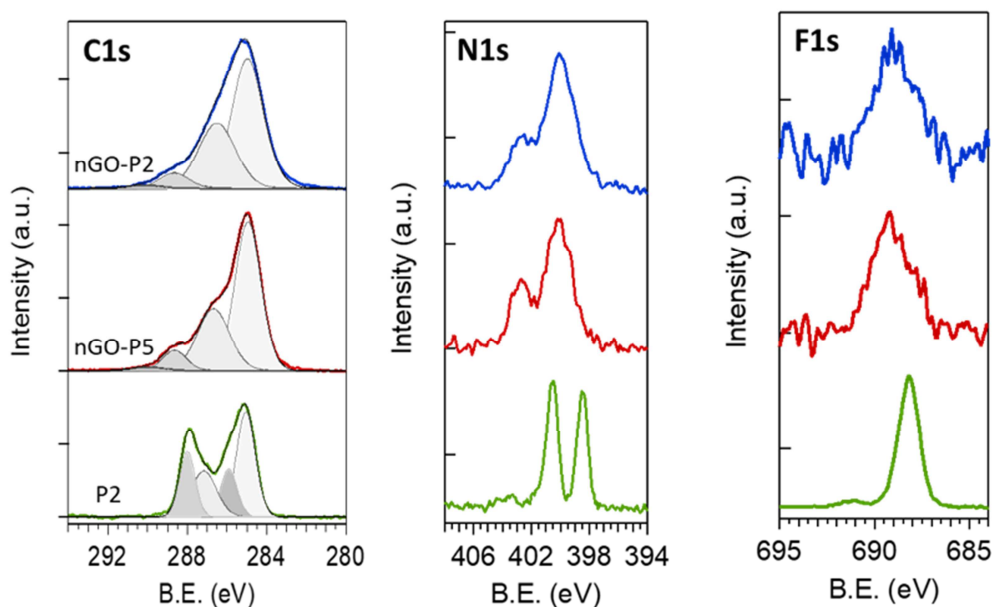


Figure 8. High-resolution XPS spectra of C1s, N1s and F1s for nanoGO-**P2**, nanoGO-**P5** and porphyrin **P2**.

The morphologies of nanoGO-**P2** and **P5** hybrids have been analysed by TEM in comparison with pristine nano-GO (Figure 9). The TEM images of these materials in Figure 9 (B) and (C) show that their surface presented a wrinkled texture with scrolled edges and broad dark spots. Although some nano-sheets tend to aggregate during the drying process, the darker areas observed in the hybrids are in higher amount when compared with pristine nano-GO sheets (Figure 9 (A)). According with the literature these dark spots are due to some degree of sheet folding resulting from coupling of nano-GO with the glycol porphyrins [58-59] and additionally to aggregation induced by the porphyrin brushes. This clearly illustrate the successful attachment of the glycol porphyrin molecules on nanoGO-CO₂H.

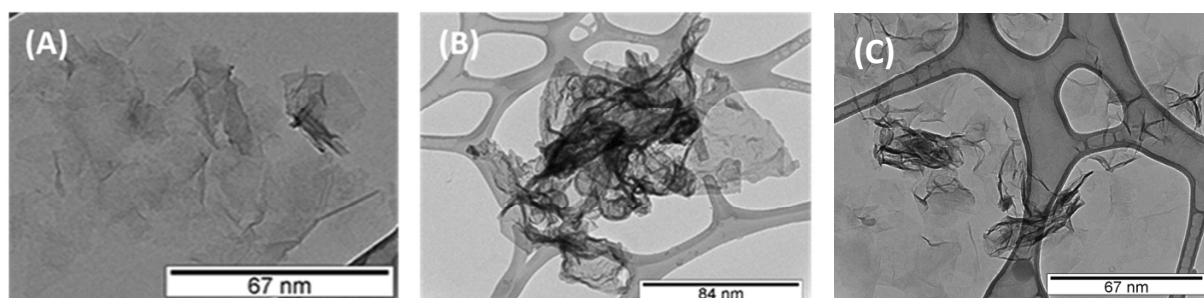


Figure 9. TEM images of nano-GO (A), nanoGO-P2 (B) and nanoGO-P5 (C).

An additional evidence of the successful functionalization of glycol porphyrins with nano-GO was obtained from TGA under inert atmosphere. Figure 10 shows the thermogravimetric profiles of nanoGO-CO₂H, nanoGO-P5 and porphyrin P5. The TGA curve of nanoGO-CO₂H indicates that it is a multistep process as reported in the literature [60]. The weight loss detected in the range of 50–180°C (8%) is attributed to the elimination of physisorbed water on the nanoGO-CO₂H surface. Further thermal decomposition is observed between 220–600°C (weight loss of 20%). Such a weight loss may be attributed to the decarboxylation, decomposition of –OH that are bound on the surface of nanoGO-CO₂H [61-62]. For nanoGO-P5, and P5 an additional weight loss of 25% was observed at 500°C, which can be assigned to the removal of pyrrole groups and complete decomposition of macrocyclic ligand [63-64]. A similar behavior was observed for nanoGO-P2 (Supporting Information-Figure S15).

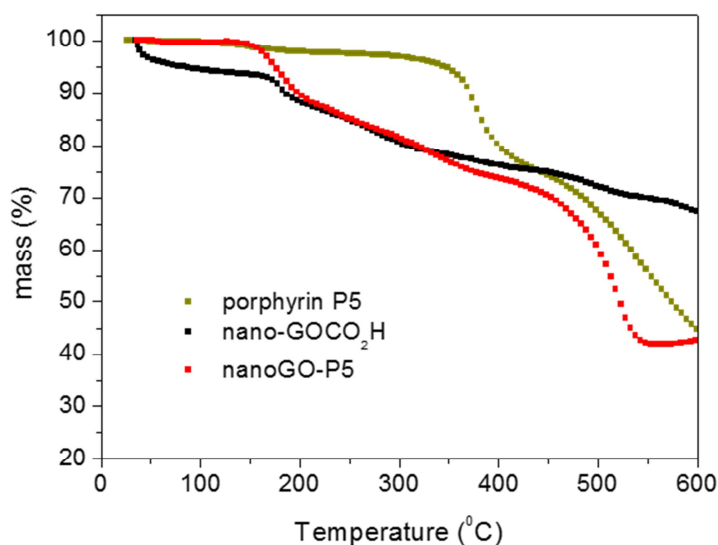


Figure 10. TGA curves of nanoGO-CO₂H, porphyrin **P5** and nanoGO-**P5**.

3.3. Biocompatibility studies with the hybrid materials nanoGO-P2, P5

Given the current interest in exploring the biomedical applications of new graphene-related hybrid nanomaterials, the cell response of human Saos-2 osteoblasts was studied in the presence of nanoGO-**P2** and nanoGO-**P5**. Several studies to assess the *in vitro* and *in vivo* biocompatibility of graphene-based nanomaterials indicate that their cytotoxicity is dependent on different physicochemical properties (shape, size, and functional groups), dispersion procedure, synthesis method, dose, administration form and exposure times [65-68].

Figure 11A shows the cell proliferation (viable cell number per mL) of Saos-2 osteoblasts cultured during 24 hours with 50 µg/mL of nanoGO-CO₂H and the hybrid nanomaterials nanoGO-**P2** and nanoGO-**P5** (**P2** and **P5**, respectively). No significant differences were observed when the cells were cultured in the presence of the different nanomaterials when compared to

control, Saos-2 cells cultured without material (Ctrl). To evaluate the possible cytotoxic effect of these new hybrid materials, the cell viability after 24 hours was also measured (Figure 11B) by the trypan blue assay, which is often used as a direct biomarker of the cellular plasma membrane integrity. The results indicated very high viability percentages in all studied cases, without any significant differences with respect to control cells (~ 99.7% of viability). Specifically, the viability values obtained were ~ 99.4%, ~ 99.2% and ~ 99.3% for nanoGO-CO₂H, nanoGO-P2 and nanoGO-P5, respectively. All these values are indicative of healthy cell cultures, where the plasma membrane integrity is preserved after 24 hours of exposure to 50 µg/mL of hybrid nanomaterials. The results for the positive control (1% Triton X-100, 10 min) showed 100% cell mortality. Thus, the obtained results highlight that human Saos-2 osteoblasts exposed during 24 hours to 50 µg/mL of graphene-based hybrid nanomaterials proliferate in a similar way to control cells cultured without nanomaterial. Moreover, the high viability values showed by this cell type after culture with these new hybrid nanomaterials emphasize that the dose used in the study as well as their surface charge and size did not induce cellular plasma membrane damage, maintaining its integrity.

A cell biomarker related to oxidative stress and cell cytotoxicity is the intracellular reactive oxygen species (ROS) production. Figure 11C shows the intracellular ROS production by human Saos-2 osteoblasts cultured with 50 µg/mL of nanoGO-CO₂H, and of hybrids nanoGO-P2 and nanoGO-P5 during 24 hours, with respect to percentage of control condition (cell culture without material). No significant differences were observed when Saos-2 tumor cells were cultured in the presence of the different nanomaterials compared to control cells (Ctrl), but a slight decrease in the intracellular ROS production is observed in the nanoGO-Px hybrids when compared to control cells. Cells exposed to H₂O₂ (positive control for ROS) presented an increase in ROS production of ≈ 40%.

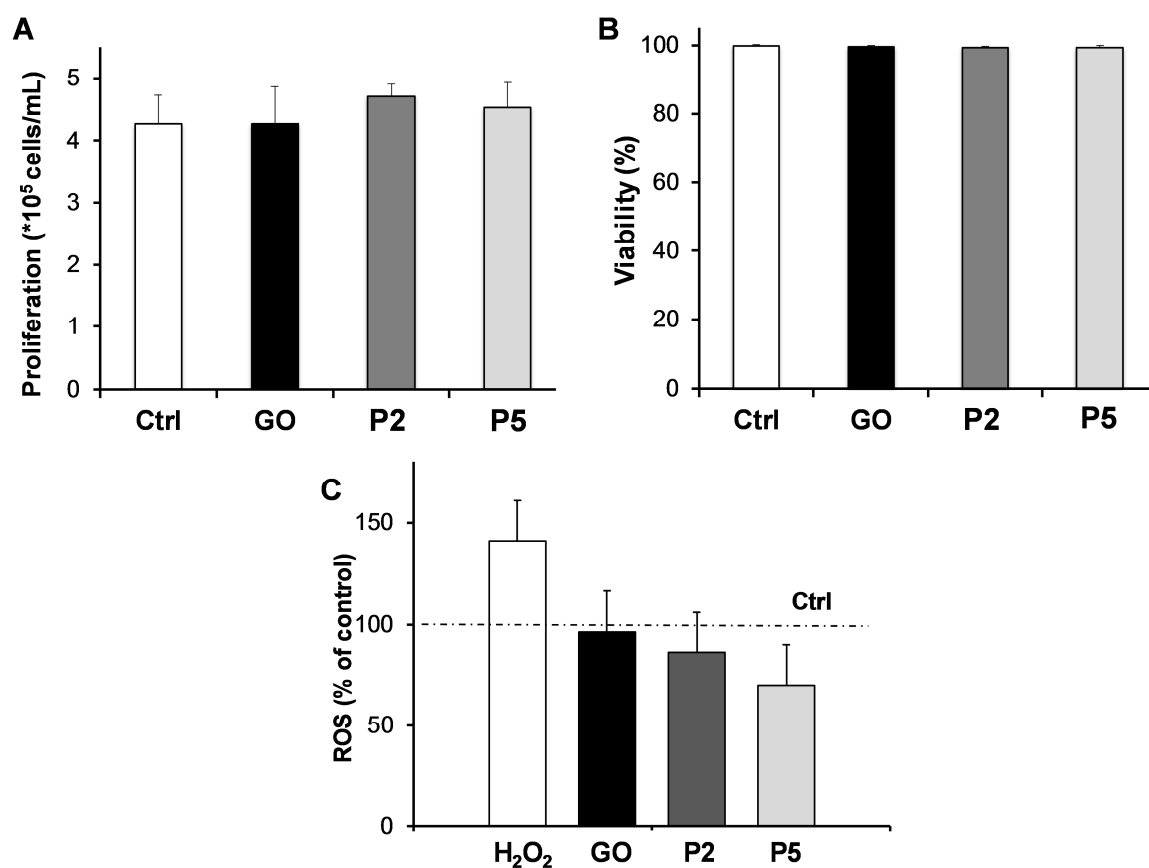


Figure 11. Human saos-2 sarcoma osteoblasts cultured without (Ctrl) and with 50 $\mu\text{g/mL}$ of nanoGO-CO₂H (GO) or hybrid nanomaterials (nanoGO-P2, (P2) and nanoGO-P5 (P5)) during 24 hours. (A) Cell proliferation expressed as $\times 10^5$ viable cells/mL. (B) Cell viability expressed as percentage. (C) Intracellular ROS production, using the DCFDA assay. As positive control for ROS, cells were exposed to 140 μM H₂O₂ for 24 h. The results were expressed as the mean \pm SD expressed as % of control.

Several studies proposed oxidative stress as a key mechanism involved in the toxicity of various graphene-based nanomaterials resulting from the imbalance between excessive generation of ROS and the limited antioxidant defence capacity of cells, thereby leading to adverse biological

effects such as damage of biomolecules, *e.g.*, peroxidation of membrane lipids, denaturation of proteins and alterations in DNA. In particular, graphene oxide increased the formation of intracellular ROS in both A549 and RAW 264.7 cells at a concentration of 12.5 $\mu\text{g}/\text{cm}^2$ up to 3.5-times compared to control cells, after 30 min of exposure [69]. Another study demonstrate that Saos-2 osteoblasts, MC3T3-E1 preosteoblasts and RAW-264.7 macrophages cultured with 75 $\mu\text{g}/\text{mL}$ of GO nanosheets decorated with 1-arm and 6-arm PEG presented an increase intracellular ROS content after 24 hours [70]. However, in our experimental conditions the results shown in Figure 11C emphasize that the exposure to 50 $\mu\text{g}/\text{mL}$ of such graphene-based hybrid nanomaterials during 24 hours did not induce intracellular ROS accumulation in human Saos-2 osteoblasts. Thus, proliferation, viability and ROS generation results demonstrate the excellent biocompatibility of the graphene-based hybrid nanomaterials tested.

Forward angle (FSC) and side angle (SSC) scatters are indicative of cell size and complexity, respectively. Figure 12 shows the FSC vs SSC scatters of control Saos-2 cells (Figure 12A) and human Saos-2 cells cultured with 50 $\mu\text{g}/\text{mL}$ of the hybrid nanomaterials nanoGO-**P2** and nanoGO-**P5** (Figure 12B and 12C, respectively). We observed an increase in both cell size (FSC) and internal complexity (SSC) of Saos-2 cells cultured in the presence of hybrid nanomaterials (nanoGO-**P2** and nanoGO-**P5** conditions) when compared to control cells. Moreover, it is also noticed that this increase is higher in osteoblast cells cultured in the presence of nanoGO-**P5** hybrid nanomaterial when compared to nanoGO-**P2** condition.

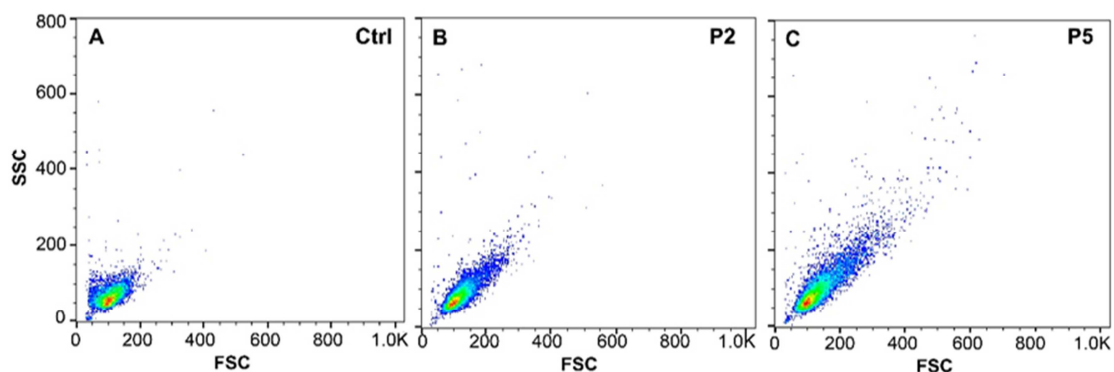


Figure 12. Effect of hybrid nanomaterials on light scattering properties of human Saos-2 sarcoma osteoblasts after 24 hours of treatment. Forward angle scatter (FSC, cell size) vs side angle light scatter (SSC, internal complexity) of control (**A**), **P2** (**B**) and **P5** (**C**) conditions.

On the other hand, the FSC and SSC scatters of control Saos-2 cells and human Saos-2 cells cultured with 50 $\mu\text{g}/\text{mL}$ of nanoGO-CO₂H are shown in Figure S16A and S16B (Supporting Information), respectively. Again, in this condition, we observed an increase in both cell size (FSC) and internal complexity (SSC) of Saos-2 cells cultured in the presence of this nanomaterial when compared to control cell.

Figure 13 shows the flow cytometric light scatter profiles (SSC) and the mean SSC (**Inset**) of human Saos-2 sarcoma osteoblasts cultured with 50 $\mu\text{g}/\text{mL}$ of hybrid nanomaterials (nanoGO-**P2** and nanoGO-**P5**) compared to control Saos-2 cells. The SSC profiles display a clear displacement towards the right for nanoGO-**P2** (blue profile) and nanoGO-**P5** (orange profile) conditions when compared to control Saos-2 cells (red profile). This displacement is accompanied by a significant increment of $\sim 30\%$ and $\sim 44\%$ in the intracellular complexity (SSC) of Saos-2 cultured with nanoGO-**P2** and nanoGO-**P5** hybrid nanomaterials respectively, compared to control condition (Inset in Figure 13). Moreover, there is also a significant increment of $\sim 12\%$ in the intracellular complexity of Saos-2 osteoblasts cultured with nanoGO-

P5 hybrid nanomaterial when compared to nanoGO-**P2** condition. On the other hand, SSC profiles and SSC mean of human Saos-2 sarcoma osteoblasts cultured with 50 $\mu\text{g}/\text{mL}$ of nanoGO-CO₂H compared to control Saos-2 cells are shown in Figure S16C and inset, respectively. In this case, there is also a clear displacement towards the right in the SSC profile of Saos-2 cells cultured with nanoGO-CO₂H when compared to control cells which is accompanied by a significant increment of $\sim 26\%$ in the internal complexity of osteoblasts.

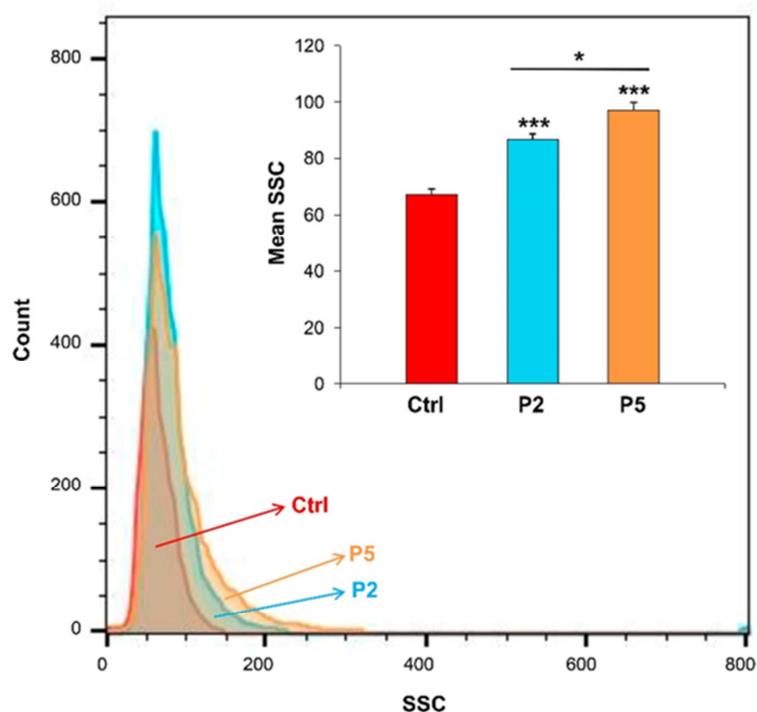


Figure 13. Cell uptake of hybrid nanomaterials. (A) Side angle light profiles (SSC, internal complexity) vs number of human Saos-2 sarcoma osteoblasts after 24 hours of culture in the absence of material (red profile) and cultured in **P2** or **P5** conditions (blue and orange profiles, respectively). (Inset) Graph bar presents the geometric mean for SSC parameter as mean \pm SD, for the culture conditions tested. Significant statistical $*p < 0.05$ and $***p < 0.005$.

The use of graphene-based hybrid nanomaterials for different biomedical applications as therapeutics delivery, photodynamic therapy for clinical treatment of several types of cancer, among other, requires that such nanomaterials have to be incorporated by the cells without provoking cell structural and functional alterations. Flow cytometric light scatter analysis is a simple and easy method to evaluate uptake potential of nanomaterials by mammalian cells [38]. Thus, the amount of hybrid nanomaterials taken up by the Saos-2 tumor cells after 24 hours of culture was analysed using light scatter analysis. The results shown in Figure 12 and Figure 13 highlight that these hybrid nanomaterials with a size of 160-190 nm and a surface charge of ~30 mV (Supporting Information, Figure S17) have been incorporated by Saos-2 tumor cells, since that a significant increase both cell size and intracellular complexity was observed after 24 hours of culture with these nanomaterials dispersed in the medium. Similarly, it was previously demonstrated that PEGylated-GO nanosheets (*ca.* 100 nm) were incorporated by mammalian cells after 24 hours of exposure. Moreover, it was described that the incorporation of these nanosheets into Saos-2 osteoblasts was mainly due to macropinocytosis and that this nanomaterial could also enter through pathways dependent on microtubules [15].

Finally, Saos-2 osteoblasts incorporate more nanoGO-**P5** than nanoGO-**P2** hybrid nanomaterials. This higher incorporation should be related to their physicochemical properties, in particular the fact that the longer glycol chains prevent aggregation of the porphyrins.

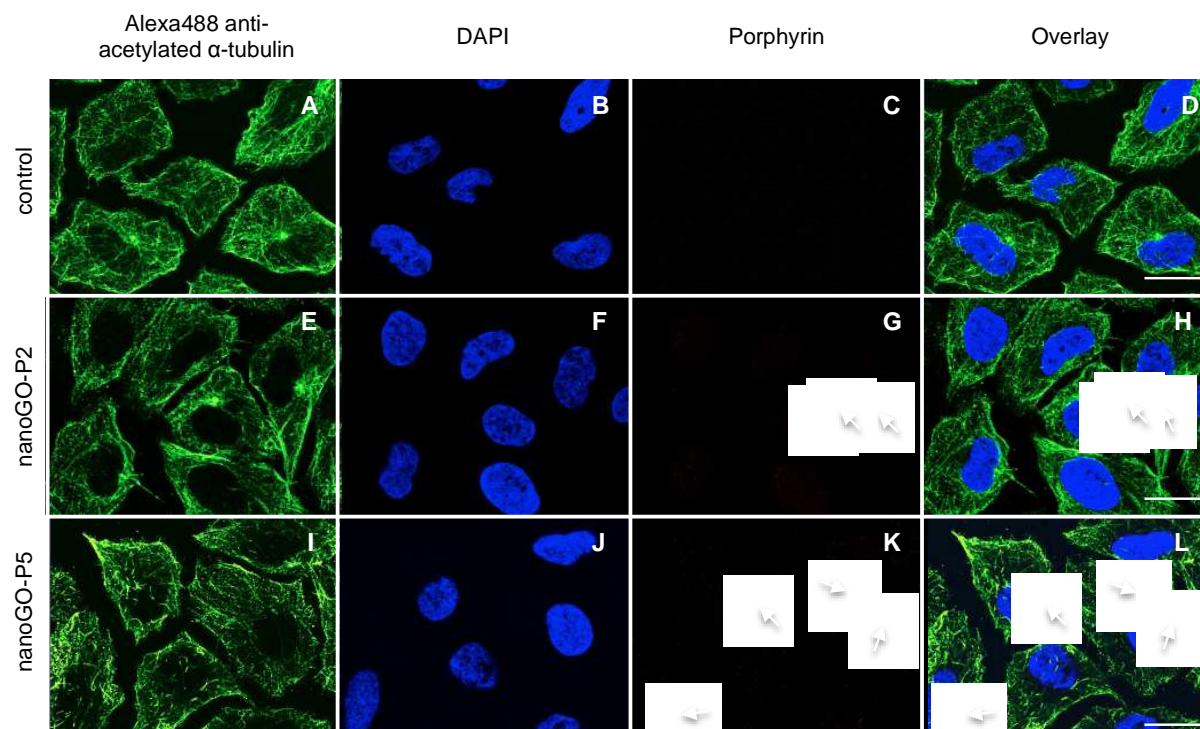


Figure 14. Morphology evaluation by confocal microscopy of cultured human Saos-2 osteoblasts after 1-day treatment with nanoGO-porphyrin hybrids. Panels **A-D** correspond to a control experiment where the cells were cultured without nanoGO-Px, panels **E-H** and **I-L** show the cells cultured in the presence of nanoGO-P2 and nanoGO-P5, respectively. Cells were delimited by staining with anti-acetylated α -tubulin antibody and green fluorescing Alexa Fluor 488-secondary antibody to detect microtubules (panels **A**, **E** and **I**), nuclei were stained with blue fluorescing DAPI (panels **B**, **F** and **J**), and red fluorescing porphyrin was used for the visualization of the hybrid nanomaterials (panels **G** and **K**). A nuclear transversal focal plane is presented showing the internalized porphyrin (arrows) and the nucleus. Scale bar = 20 μ m.

The cellular morphology and the intracellular localization of the nanomaterial was evaluated by confocal microscopy. Figure 14 shows confocal microscopy images of Saos-2 tumor cells

cultured without any nanomaterial (panels **A-D**) and cultured in the presence of 50 $\mu\text{g/mL}$ of nanoGO-**P2** (panels **E-H**) and **P5** hybrid nanomaterials (panels **I-L**). We observe that Saos-2 cells cultured during 24 hours in the presence of these hybrid nanomaterials have a morphology similar to control cells, with all cells presenting the expected arrays of stable microtubules of viable cells. Moreover, panels **G** and **K** show emission of the porphyrin (650-754 nm) featuring the internalization of the nanomaterial by the cell and its preferential localization in the perinuclear area, clearly outside of the nucleus, as it is indicated by white arrows. By immunostaining the intracellular collagen of Saos-2 cells, that is highly abundant in the Golgi, we observed that the hybrid nanomaterials localize near this organelle (Supplementar Figure S18). No apparent signs of nuclear shrinkage (pyknosis) were observed. Saos-2 osteoblasts appeared “healthy”, *i.e.*, no modification of their morphology was found when compared to untreated control cells, as denoted by their intact microtubular and actin cytoskeletons (Figure 14 and Supplementar Figure S18). Cell distribution of nanomaterials is critically dependent on the cell type and their lateral dimension, among other. Matesanz *et al.* described a F-actin co-localization of the PEGylated-GO nanosheets (*ca.* 100 nm) in Saos-2 osteoblasts, MC3T3-E1 preosteoblasts and RAW-264.7 macrophages [70]. Horváth *et al.*, observed that graphene oxide, with lateral dimensions up to several microns was internalized by epithelial cells and macrophages and are located within structures surrounded by membranes, likely (endo)lysosomal compartments [69]. The obtained results demonstrate the biocompatibility of hybrid nanomaterials which is an interesting finding to continue the study of the potential biomedical application of these new graphene-based hybrid nanomaterials. Substantial work remains in elucidating detailed mechanisms of how the relevant parameters (*e.g.*, shape, surface

properties) of these new hybrid nanomaterials affect humans or animal models, at the cellular level, at the level of organs and ultimately, the whole organism.

4. Conclusions

In summary, we report the successful incorporation of two series of porphyrins bearing different number of ethylene glycol or tetraethylene glycol chains in nano-GO functionalized with extra carboxylic groups through ester bonds. The results of FTIR, Raman, XPS, UV-vis and morphological studies confirm the success of the covalent functionalization of nanoGO-CO₂H with glycol porphyrins. The resultant hybrid nanomaterials, in particular nanoGO-P2 and nanoGO-P5 showed an improved water dispersibility and stability during long periods of time, that is a necessary requirement for their use in biomedical applications.

Biocompatibility results highlight that human Saos-2 osteoblasts exposed to 50 µg/mL of graphene-related hybrid nanomaterials for 24 hours proliferate in a similar way to control cells. Moreover, the high viability values showed by this cell type after culture with those nanomaterials emphasize that the dose used in this study as well as their surface charge and size did not induce cellular plasma membrane damage maintaining its integrity during the cell uptake process. A slight decrease in the intracellular ROS production was observed for the hybrids when compared to the non-functionalized nano-GO. The hybrid nanomaterials appear to localize preferentially in the perinuclear area. The biocompatibility results provide interesting findings to continue the study of the potential application of these new graphene-related hybrid nanomaterials for cancer therapy.

Acknowledgments

Authors are grateful to Fundação para a Ciência e Tecnologia (FCT, Portugal), European Union, QREN, FEDER and COMPETE for funding the QOPNA, TEMA, CQFM and iBiMED research units (project Pest-C/QUI/UI0062/2013, UID/EMS/00481/2013, UID/NAN/50024/2013, UID/BIM/04501/2013) and the Portuguese National NMR and PPBI Bioimaging Networks, also supported by funds from FCT (POCI-01-0145-FEDER-022122). FCT is acknowledged for the Post-Doctoral grants of C.I.M.S., M.C., I.M., V.S.S. and H.O. and for supporting the individual work contract of E.M. and P.A.A.P.M within the Investigador FCT program (SFRH/BPD/105478/2014, SFRH/BPD/101468/2014, SFRH/BPD/75782/2011, SFRH/BPD/110269/2015, SFRH/BPD/111736/2015, IF/00759/2013 and IF/00917/2013).

References

-
- [1]G. Gonçalves, M. Vila, M. T. Portolés, M. Vallet-Regi, J. Gracio, P. A. A. P. Marques, Nano-graphene oxide: a potential multifunctional platform for cancertherapy, *Adv. Healthc. Mater* 2 (8) (2013) 1072-90.
- [2]G. Gonçalves, M. Vila, I. Bdikin, A. Andrés, N. Emami, R. A. S Ferreira, et al., Breakdown into nanoscale of graphene oxide: Confined hot spot atomic reduction and fragmentation, *Scientific Reports* (4) (2014) 6735-6743.
- [3]W. Zhang, S. Wang, J. Ji, Y. Li, G. Zhang, F. Zhang, et al., Primary and tertiary amines bifunctional graphene oxide for cooperative catalysis, *Nanoscale* 5 (13) (2013) 6030-6033.
- [4]K. Yang, L. Feng, H. Hong, W. Cai, Z. Liu, Preparation and functionalization of graphene nanocomposites for biomedical applications, *Nat. Protoc* 8 (2013) 2392-2403.
- [5]A. Jaggernauth, R. M. Silva, M. A. Neto, M. J. Hortigüela, G. Goncalves, M. K. Singh, et al., Nanographene Oxide Functionalization with Organic and Hybrid Organic–Inorganic Polymers by Molecular Layer Deposition, *J. Phys. Chem. C* 120 (42) (2016) 24176-24186.
- [6]V. Georgakilas, J. N. Tiwari, K. C. Kemp, J. A. Perman, A. B. Bourlinos, K. S. Kim, Noncovalent Functionalization of Graphene and Graphene Oxide for Energy Materials, Biosensing, Catalytic, and Biomedical Applications, *Chem. Rev* 116 (9) (2016) 5464-5519.
- [7]G. Reina, J. M. González-Domínguez, A. Criado, E. Vázquez, A. Bianco, A. Prato, Promises, facts and challenges for graphene in biomedical applications, *Chem. Soc. Rev.* 46 (15) (2017) 4400-4416.
- [8]K. Yang, L. Feng; X. Shi, Z. Liu, Nano-graphene in biomedicine: theranostic applications, *Chem. Soc. Rev.* 42 (2) (2013) 530-547.

-
- [9]Y. Liu, J. Zhou, X. Zhang, Z. Liu, X. Wan, J. Tian, et al., Synthesis, characterization and optical limiting property of covalently oligothiophene-functionalized graphene material, *Carbon* 47 (13) (2009) 3113-3121.
- [10]L. Valentini, M. Cardinali, S. B. Bon, D. Bagnis, R. Verdejo, M. A. Lopez-Manchado, et al., Use of butylamine modified graphene sheets in polymer solar cells, *J. Mater. Chem* 20 (5) (2010) 995-1000.
- [11]Z. M. Markovic, L. M. Harhaji-Trajkovic, B. M. T. Markovic, D. P. Kepic, K. M. Arsikin, S. P. Jovanovic, In vitro comparison of the photothermal anticancer activity of graphene nanoparticles and carbon nanotubes, *Biomaterials* 32 (4) (2011) 1121-1129.
- [12]C. Brown, Targeted therapy: An elusive cancer target, *Nature* 537 (2016) S106-8.
- [13]Z. Liu, J. T. Robinson, X. M. Sun, H. J. Dai, PEGylated Nanographene Oxide for Delivery of Water-Insoluble Cancer Drugs, *J. Am. Chem. Soc.* 130 (33) (2008) 10876-10877.
- [14]M. Kakran, N. G. Sahoo, H. Bao, Y. Pan, L. Li, Functionalized graphene oxide as nanocarrier for loading and delivery of ellagic acid, *Curr. Med. Chem* 18 (29) (2011) 4503-4512.
- [15]X. Yan, G. Niu, J. Lin, A. J. Jin, H. Hu, Y. Tang, et al., Enhanced fluorescence imaging guided photodynamic therapy of sinoporphyrin sodium loaded graphene oxide, *Biomaterials* 42 (15) (2015) 94-102.
- [16]Y. Li, H. Dong, Y. Li, D. Shi, Graphene-based nanovehicles for photodynamic medical therapy, *International Journal of Nanomedicine* 10 (1) (2015) 2451-2459.
- [17]R. Imani, W. Shao, S. H. I. Emami, S. Faghihi, S. Prakash, Improved dispersibility of nano-graphene oxide by amphiphilic polymer coatings for biomedical applications, *RSC Adv* 6 (81) (2016) 77818-77829.

-
- [18]C. Peng, W. Hu, Y. Zhou, C. Fan, Q. Huang, Intracellular imaging with a graphene-based fluorescent probe, *Small* 6 (15) (2010) 1686-1692.
- [19]X. Sun, Z. Liu, K. Welsher, J. T. Robinson, A. Goodwin, S. Zaric ,et al., Nano-Graphene Oxide for Cellular Imaging and Drug Delivery, *Nano Res* 1 (3) (2008) 203-212.
- [20]P. Rong, K. Yang, A. Srivastan, D. O. Kiesewetter, X. Yue, F. Wang, Photosensitizer loaded nano-graphene for multimodality imaging guided tumor photodynamic therapy, *Theranostics* 4 (3) (2014) 229-239.
- [21]K. Yang, J. Wan, S. Zhang, B. Tian, Y. Zhang, Z. Liu, The influence of surface chemistry and size of nanoscale graphene oxide on photothermal therapy of cancer using ultra-low laser power, *Biomaterials* 33 (7) (2012) 2206-2214.
- [22]J. Linares, M. C. Matesanz, M. Vila, M. J. Feito, G. Goncalves, M. V. Regí, et al., Endocytic mechanisms of graphene oxide nanosheets in osteoblasts, hepatocytes and macrophages, *ACS Appl. Mater. Interfaces* 6 (16) (2014) 13697-13706.
- [23]M. Vila, M. T. Portolés, P. A. A. P. Marques, M. J. Feito, M. C. Matesanz, C. Ramírez-Santillán, et al., Cell uptake survey of pegylated nanographene oxide, *Nanotechnology* 23 (46) (2012) 465103.
- [24]S. Singh, A. Aggarwal, N. V. S. D. Bhupathiraju, G. Arianna, K. Tiwari, C. M. Drain, Glycosylated Porphyrins, Phthalocyanines, and other Porphyrinoids for Diagnostics and Therapeutics, *Chem. Rev* 115 (18) (2015) 10261-10306.
- [25]M. Ethirajan, Y. Chen, P. Joshi, R. K. Pandey, The role of porphyrin chemistry in tumor imaging and photodynamic therapy, *Chem. Soc. Rev* 40 (1) (2011) 340-362.

-
- [26]Y. Xu, Z. Liu, X. Zhang; Y. Wang, J. Tian, Y. Huang, et al., Graphene Hybrid Material Covalently Functionalized with Porphyrin: Synthesis and Optical Limiting Property, *Adv. Mater* 21 (12) (2009) 1275-1279.
- [27]A. Wang, W. Yu, Z. Xiao, Y. Song, L. Long, M. P. Cifuentes, et al., A 1,3-dipolar cycloaddition protocol to porphyrin-functionalized reduced graphene oxide with a push-pull motif, *Nano Res* 8 (3) (2015) 870-886.
- [28]S. Su, J. Wang, J. Wei, R. Martínez-Zaguila, J. Qiu, S. Wang, Efficient Photothermal Therapy of Brain Cancer through Porphyrin Functionalized Graphene Oxide, *New J. Chem* 39 (7) (2015) 5743-5749.
- [29]J. Xu, F. Zeng, H. Wu, C. Yu, S. Wu, Dual-targeting nanosystem for enhancing photodynamic therapy efficiency, *Appl. Mater. Interfaces* 7 (17) (2015) 9287-9296.
- [30]Y. Cao, H. Dong, Z. Yang, X. Zhong, Y. Chen, W. Dai, et al., Aptamer-Conjugated Graphene Quantum Dots/Porphyrin Derivative Theranostic Agent for Intracellular Cancer-Related MicroRNA Detection and Fluorescence-Guided Photothermal/Photodynamic Synergetic Therapy, *ACS Appl. Mater. Interfaces* 9 (1) (2017) 159-166.
- [31]G. Eda, G. Fanchini, M. Chhowalla, Large-area ultrathin films of reduced graphene oxide as a transparent and flexible electronic material, *Nat. Nanotechnol* 3 (2008) 270-274.
- [32]R. Imani, S. H. Emami, S. Faghihi, Nano-graphene oxide carboxylation for efficient bioconjugation applications: a quantitative optimization approach, *J Nanopart Res* 17 (2015) 88.

-
- [33]K. A. D. F. Castro, M. M. Q. Simões, M. G. P. M. S. Neves, J. A. S. Cavaleiro, F. Wypych, S. Nakagaki, Glycol metalloporphyrin derivatives in solution or immobilized on LDH and silica: synthesis, characterization and catalytic features in oxidation reactions, *Catal. Sci. Technol* 4 (1) (2014) 129-141.
- [34]T. Foroutan, N. Nazemi, M. Tavana, M. Z. Kassaei, E. Motamedi, S. Sonieshargh, et al, Suspended graphene oxide nanoparticle for accelerated multilayer osteoblast attachment, *J Biomed Mater Res Part A (106 A)* (2018) 293–303.
- [35]M. Kalbacova, A. Broz, J. Kong, M. Kalbac, Graphene substrates promote adherence of human osteoblasts and mesenchymal stromal cells, *Carbon* 48 (2010) 4323 – 4329.
- [36]F. F. C. Torres, A. R. Galván, C. E.G. Beltrán, E. M. Lorán, E. V. Garza, N. O. Soto, et al Differential cytotoxicity and internalization of graphene family nanomaterials in myocardial cells, *Mater Sci Eng C Mater Biol Appl* 73 (2017) 633-642.
- [37]W. Yu, J. Zhu, Y. Wang, J. Wang, W. Fang, K. Xia, et al, A review and outlook in the treatment of osteosarcoma and other deep tumors with photodynamic therapy: from basic to deep, *Oncotarget* 8 (24) (2017) 39833-39848.
- [38]H. Suzuki, T. Toyooka, Y. Ibuki, Simple and Easy Method to Evaluate Uptake Potential of Nanoparticles in Mammalian Cells Using a Flow Cytometric Light Scatter Analysis, *Environ. Sci. Technol* 41 (8) (2007) 3018-3024.
- [39]C. Greulich, J. Diendorf, T. Simon, G. Eggeler, M. Epple, Uptake and intracellular distribution of silver nanoparticles in human mesenchymal stem cells, *Acta Biomater* 7 (1) (2011) 347-354.

-
- [40]J. M. Udall, R. A. Moscicki, F. I. Preffer, P. D. Ariniello, E. A. Carter, A. K. Bhan, et al., Flow cytometry: a new approach to the isolation and characterization of Kupffer cells, *Adv. Exp. Med. Biol* 216 (1987) 821.
- [41]S. Niyosi, E. Bekyanova, M. E. Itkis, J. L. Mcwilliams, M. A. Haman, R. C. Haddon, Solution properties of graphite and graphene, *J. Am. Chem. Soc* 128 (24) (2006) 7720-7721.
- [42]L. Zhao, S. T. Yang, S. Feng, Q. Ma, X. Peng, D. Wu, Preparation and application of carboxylated graphene oxide sponge in dye removal, *Int. J. Environ. Res. Public Health* 14 (2017) 1301-1314.
- [43]L. Yu, P. Lia, X. Ding, Q. Zhang, Graphene oxide and carboxylated graphene oxide: Viable two-dimensional nanolabels for lateral flow immunoassays, *Talanta* 165 (2017) 167–175.
- [44]E. M. S. Maçôas, R. Fausto, J. Lundell, M. Pettersson, L. Khriachtchev, M. Rasanen, A matrix isolation spectroscopic and quantum chemical study of fumaric and maleic acid, *J. Phys. Chem. A* 105 (15) (2011) 3922-3933.
- [45]T. Rattanaa, S. Chaiyakuna, N. Witit-anuna, N. Nuntawongb, P. Chindaudomb, S. Oaewc, et al., Preparation and characterization of graphene oxide nanosheets, *Procedia Engineering* 32 (2012) 759-764.
- [46]K. Nakamoto, *Infrared and Raman spectra of inorganic and coordination compounds parts A and B*, Wiley Interscience Publication, 5th edn, (1997).
- [47]S. Peng, C. Liu, X. Fan, Surface modification of graphene oxide by carboxyl-group: Preparation, characterization, and application for proteins immobilization, *Integrated Ferroelectrics* 163 (1) (2015) 42-53.

- [48]V. Villari, P. Mineo, E. Scamporrino, N. Micali, Spontaneous self-assembly of water-soluble porphyrins having poly(ethyleneglycol) as branches: Dependence of aggregate properties from the building block architecture, *Chemical Physics* 409 (2012) 23–31.
- [49]A. Wang, L. Long, L. Zhao, W. M. G. Humphrey, M. P. Cifuentes, C. Zhang, Increased optical nonlinearities of graphene nanohybrids covalently functionalized by axially-coordinated porphyrins, *Carbon* 53 (2013) 327-338.
- [50]A. Wang, W. Yu, Z. Huang, F. Zhou, J. Song, Y. Song, et al., Covalent functionalization of reduced graphene oxide with porphyrin by means of diazonium chemistry for nonlinear optical performance, *Scientific Reports* 6 (2016) 23325.
- [51]W. Song, C. He, Y. Dong, W. Zhang, Y. Gao, Y. Wu, et al., The effects of central metals on the photophysical and nonlinear optical properties of reduced graphene oxide–metal(II) phthalocyanine hybrids, *Phys. Chem. Chem. Phys* 17 (11) (2015)7149-7157.
- [52]V. V. Serra, S. M. Andrade, M. G. P. M. S. Neves, J. A. S Cavaleiro; S. M. B. Costa, J-aggregate formation in bis-(4-carboxyphenyl)porphyrins in water : pH and counterion dependence, *New J. Chem* 34 (12) (2010) 2757-2765.
- [53]C. Zhong, J. Wang, Z. Chen, H. Liu, SnO₂–Graphene Composite Synthesized via an Ultrafast and Environmentally Friendly Microwave Autoclave Method and Its Use as a Superior Anode for Lithium-Ion Batteries, *J. Phys. Chem. C* 115 (56) (2011) 25115-25120.
- [54]R. Gea, X. Wanga, C. Zhanga, S. Kanga, L. Qina, G. Li, et al., The influence of combination mode on the structure and properties of porphyrin–graphene oxide composites, *Colloids and Surfaces A: Physicochem. Eng. Aspects* 483 (2015) 45-52.

- [55]N. A. Kumar, R. R. Gaddam, M. Suresh, S. R. Varanasi, D. Yang, S. K. Bhatiaa, et al, Porphyrin–graphene oxide frameworks for long life sodium ion batteries, *J. Mater. Chem. A* 5 (2017) 13204-13211.
- [56]Y. Du, N. Dong, M. Zhang, K. Zhu, R. Na, S. Zhang, N. Sun, G. Wang, J. Wang, Covalent functionalization of graphene oxide with porphyrin and porphyrin incorporated polymers for optical limiting, *Phys. Chem. Chem. Phys* 19 (2017) 2252-2260.
- [57]A. Wang, Y. Fang, L. Long, Y. Song, W. Yu, W. Zhao, et al., Facile Synthesis and Enhanced Nonlinear Optical Properties of Porphyrin-Functionalized Multi-Walled Carbon Nanotubes, *Chem. Eur. J* 19 (42) (2013) 14159-14170.
- [58]N. Karousis, A. S. D. Sandanayaka, T. Hasobe, S. P. Economopoulos, E. Sarantopoulou, N. Agmatarchis, Graphene oxide with covalently linked porphyrin antennae: Synthesis, characterization and photophysical properties, *J. Mater. Chem* 21 (1) (2011) 109-117.
- [59]X. Zhang, Y. Feng, S. Wang, W. Feng, Preparation of a graphene oxide-phthalocyanine hybrid through strong π - π interactions, *Carbon* 48 (1) (2010) 211-216.
- [60]R. Yamuna, S. Ramakrishnan, K. Dhara, R. Devi, N. K. Kothurkar, E. Kirubha, et al, Synthesis, characterization, and nonlinear optical properties of graphene oxide functionalized with tetra-amino porphyrin, *J Nanopart Res*, 15 (2013) 1399.
- [61]V. H. Pham, H. D. Pham, T. T. Dang, S. H. Hur, E. J. Kim, B. S. Kong, et al, Chemical reduction of an aqueous suspension of graphene oxide by nascent hydrogen, *J. Mater. Chem* 22 (2012) 10530-10536.
- [62]V. Basiuk, M. M. Herrera, E. A. Zauco, L. V. H. Holguín, I. P. Lee, V. A. Basiuk, Noncovalent functionalization of graphene with a Ni(II) tetraaza[14]annulene complex, *Dalton Trans* 43 (20) (2014) 7413-7428.

-
- [63]A. M. Al-Sabagha, M. A. Betihaa, D. I. Osmana, A. I. Hashimb, M. M. E. Sukkarya, T. Mahmoud, Preparation and Evaluation of Poly(methyl methacrylate)-Graphene Oxide Nanohybrid Polymers as Pour Point Depressants and Flow Improvers for Waxy Crude Oil, *Energy Fuels* 30 (9) (2016) 7610-7621.
- [64]G. D. Bajju, S. Kundan, M. Bhagat, D. Gupta, A. Kapahi, G.Devi, Synthesis and Spectroscopic and Biological Activities of Zn(II) Porphyrin with Oxygen Donors, *Bioinorganic Chemistry and Applications* 782762 (2014) 1-13.
- [65]Y. Talukdar, J. T. Rashkow, G. Lalwani, S. Kanakia, B. Sitharaman, The effects of graphene nanostructures on mesenchymal stem cells, *Biomaterials* 35 (18) (2014) 4863-4877.
- [66]H. Yue, W. Wei, Z. Yue, B. Wang, N. Luo, Y. Gao, et al., The role of the lateral dimension of graphene oxide in the regulation of cellular responses, *Biomaterials* 33 (16) (2012) 4013-4021.
- [67]Y. Chang, S. T. Yang, J. H. Liu, E. Dong, Y. Wang, A. Cao, et al., In vitro toxicity evaluation of graphene oxide on A549 cells, *Toxicol. Lett* 200 (3) (2011) 201-210.
- [68]M. Lv, Y. Zhang, L. Liang, M. Wei, W. Hu, X. Li, et al., Effect of graphene oxide on undifferentiated and retinoic acid-differentiated SH-SY5Y cells line, *Nanoscale* 4 (13) (2012) 3861-3866.
- [69]L. Horváth, A. Magrez, M. Burghard, K. Kern, L. Forró, B. Schwaller, Evaluation of the toxicity of graphene derivatives on cells of the lung luminal surface, *Carbon* 64 (2013) 45-60.
- [70]M. C Matesanz, M. Vila, M. J. Feito, J. Linares, G. Gonçalves, M. Vallet-Regi , et al., The effects of graphene oxide nanosheets localized on F-actin filaments on cell-cycle alterations, *Biomaterials* 34 (5) (2013) 1562-1569.